inorganics

MDPI

Review

Preparation Methods and Photocatalytic Performance of Kaolin-Based Ceramic Composites with Selected Metal Oxides (ZnO, CuO, MgO): A Comparative Review

Dikra Bouras [1], Lotfi Khezami [2], Regis Barille [3], Neçar Merah [4,5], Billel Salhi [6], Gamal A. El-Hiti [7], Ahlem Guesmi [2] and Mamoun Fellah [8,*]

[1] Matter Sciences Department, Faculty of Science and Technology, University of Souk-Ahras, Souk Ahras 41000, Algeria; d.bouras@univ-soukahras.dz
[2] Department of Chemistry, College of Science, Imam Mohammad Ibn Saud Islamic University (IMSIU), P.O. Box 5701, Riyadh 11432, Saudi Arabia; lhmkhezami@imamu.edu.sa (L.K.); amalkasme@imamu.edu.sa (A.G.)
[3] MOLTECH-Anjou, Université d'Angers/UMR CNRS 6200, 2 Bd Lavoisier, 49045 Angers, France; regis.barille@univ-angers.fr
[4] Mechanical Engineering Department, King Fahd University of Petroleum and Minerals, P.O. Box 1180, Dhahran 31261, Saudi Arabia; nesar@kfupm.edu.sa
[5] Interdisciplinary Research Center for Advanced Materials, King Fahd University of Petroleum and Minerals, Dhahran 31261, Saudi Arabia
[6] Interdisciplinary Research Center of Membrane and Water Security, King Fahd University of Petroleum and Minerals, Dhahran 31261, Saudi Arabia; billel@kfupm.edu.sa
[7] Department of Optometry, College of Applied Medical Sciences, King Saud University, Riyadh 11433, Saudi Arabia; gelhiti@ksu.edu.sa
[8] Mechanical Engineering Department, Abbes Laghrour-Khenchela University, P.O. Box 1252, Khenchela 40004, Algeria
* Correspondence: mamoune.fellah@univ-khenchela.dz; Tel.: +213-660348885

Abstract: The current review examines various methods for preparing photocatalytic materials based on ceramic substrates, with a focus on incorporating metal oxides such as ZnO, CuO, and MgO. This study compares traditional mixing, co-precipitation, sol–gel, and autoclave methods for synthesizing these materials. Kaolin-based ceramics (DD3 and DD3 with 38% ZrO_2) from Guelma, Algeria, were used as substrates. This review highlights the effects of different preparation methods on the structural, morphological, and compositional properties of the resulting photocatalysts. Additionally, the potential of these materials for the photocatalytic degradation of organic dyes, specifically Orange II, was evaluated. Results indicated that ceramic/ZnO/CuO and ceramic/MgO powders prepared via traditional mixing and co-precipitation techniques exhibited significantly faster degradation rates under visible light than Cu layers deposited on ceramic substrates using solution gradient processes. This enhancement was attributed to the increased effective surface area and the size of the spherical nanoparticles obtained through these methods, which facilitated accelerated pollutant absorption. This study highlights the ease and cost-effectiveness of preparing robust layers on ceramic substrates, which are advantageous for photocatalytic applications due to their straightforward removal after filtration. Notably, DD3Z/MgO powders demonstrated superior catalytic activity, achieving complete degradation of the organic dye in just 10 min, whereas DD3Z/ZnO-CuO powders achieved 93.6% degradation after 15 min. Additionally, experiments using kaolin-based ceramics as substrates instead of powders yielded a maximum dye decomposition rate of 77.76% over 6 h using ZnO thin layers prepared via the autoclave method.

Keywords: ceramics/ZnO-CuO; ceramics/MgO; photocatalytic; autoclave; sol–gel; co-precipitation; traditional mixture

check for updates

Academic Editor: Antonino Gulino

Received: 23 March 2025
Revised: 2 May 2025
Accepted: 9 May 2025
Published: 13 May 2025

Citation: Bouras, D.; Khezami, L.; Barille, R.; Merah, N.; Salhi, B.; El-Hiti, G.A.; Guesmi, A.; Fellah, M. Preparation Methods and Photocatalytic Performance of Kaolin-Based Ceramic Composites with Selected Metal Oxides (ZnO, CuO, MgO): A Comparative Review. *Inorganics* **2025**, *13*, 162. https://doi.org/10.3390/inorganics13050162

Copyright: © 2025 by the authors. Licensee MDPI, Basel, Switzerland. This article is an open access article distributed under the terms and conditions of the Creative Commons Attribution (CC BY) license (https://creativecommons.org/licenses/by/4.0/).

1. Introduction

In recent decades, the proliferation of industrial activities has led to an alarming increase in environmental pollutants, particularly those stemming from factory operations involving dyes [1]. While essential in various industries for coloring fabrics, plastics, and other materials, these dyes often contain complex chemical compounds that are discharged as waste [2]. When improperly managed, these dye-related pollutants can cause significant environmental harm [3], contaminating water sources, soil, and air and adversely affecting ecosystems and human health [4].Water pollution has become a pressing issue in developing countries [5] due to the prevalence of textile industries dominating their economic landscapes, among other sectors [6]. These industries and agricultural practices employ harmful chemicals that find their way into water bodies [7], contributing significantly to global water contamination [8]. The discharge of dyes and toxic organic compounds from industrial and agricultural processes has a profound impact [9], polluting aquatic environments on a large scale and posing risks to aquatic life and human health through the food chain [10]. Areas where irrigation with contaminated water occurs face additional challenges [11], leading to soil pollution and associated health risks [12]. The persistence of these toxic compounds complicates their biochemical degradation [13], prompting research efforts to develop alternative and efficient methods for their removal from air and water [14]. Techniques such as microfiltration [15], electro-coagulation [16], and flocculation have been proposed for water treatment but often need to more completely degrade pollutants quickly and affordably [17].

The challenge of mitigating such environmental damage has spurred the development of innovative technologies to reduce and manage these pollutants [18]. One promising approach is photocatalysis, which leverages light to accelerate chemical reactions that break down harmful substances [19]. In photocatalysis, a photocatalyst, typically semiconductor material, absorbs photons and generates electron–hole pairs that drive the degradation of pollutants [20]. This process holds significant potential for the filtration and detoxification of polluted water and air, making it a key area of research for environmental remediation [21].

Photocatalysis emerges as a promising solution for addressing water pollution challenges [22]. This technology leverages light as a catalyst [23], integrating nanotechnology and materials science to combat environmental pollutants [24]. Photocatalytic oxidation, a key process in this field, utilizes semiconductor surfaces activated by photon energy to generate radicals that decompose organic pollutants into harmless CO_2 and H_2O [25].Ceramics have emerged as a valuable component in photocatalysis due to their stability, durability, and catalytic properties [26]. Among various ceramic materials, kaolin, a type of clay mineral, has garnered attention for its effectiveness as a catalyst [27]. Kaolin's advantages include its high surface area, thermal stability, and cost-effectiveness [28]. Its applications extend beyond photocatalysis, encompassing fields such as ceramics manufacturing and environmental engineering [29]. Kaolin's intrinsic properties make it a suitable candidate for developing photocatalytic systems aimed at pollutant degradation [30].

The choice of raw materials is crucial for developing effective photocatalytic systems [31], with ceramic membranes presenting a viable option for their stability and cost-effectiveness [32]. Clay minerals such as kaolinite have been widely studied for their potential in fabricating heterogeneous photocatalysts [33], often combined with transition metal oxides to enhance catalytic activity [34]. In this review, kaolin-based materials (DD3 and DD3Z, the latter containing 38% ZrO_2) from Guelma, Algeria, are examined for their suitability in photodegrading organic dyes [35], particularly using the dye Orange II as a test case [35]. DD3Z, enriched with zirconium oxide, demonstrates increased open porosity favorable for catalytic applications after suitable heat treatment [36].To enhance the photocatalytic performance of ceramics, researchers have explored the incorporation of various

oxides [37], including zinc oxide (ZnO) [38], copper oxide (CuO) [39], and magnesium oxide (MgO) [40]. These added oxides offer unique characteristics that improve the efficiency of the photocatalysis process. Zinc oxide, for instance, is known for its strong UV absorption and high electron–hole pair generation [41]. Copper oxide contributes to effective pollutant degradation through its ability to create reactive oxygen species [42]. Magnesium oxide enhances photocatalytic activity by improving charge separation and stability. Together, these oxides can significantly boost the performance of photocatalytic systems [43].

Recent studies have explored bimetallic and mixed metal oxide composites, demonstrating superior efficiency compared to non-metallic counterparts [44]. Zinc oxide (ZnO) [45] and copper oxide (CuO) [46] are prominent examples of transition metal oxides used in photocatalytic applications [47]. Each exhibits specific band gaps that allow for the effective degradation of organic compounds under UV or visible light irradiation [48].The preparation of photocatalytic materials involves several methods, each influencing the properties and effectiveness of the final product [48]. Standard preparation techniques include sol–gel processes/hydrothermal synthesis and co-precipitation/mixing powder methods [49]. Specifically, for depositing thin layers on ceramic substrates, dipping and autoclave methods are frequently employed [50]. Dip-coating involves immersing the ceramic substrate into a precursor solution [35], while autoclave processing uses high pressure and temperature to enhance the deposition quality [51]; for the incorporation of oxides, deposition and mixing methods are utilized to ensure a uniform distribution and optimal interaction between the ceramic base and the added oxides [52]. Various composite ceramic/metal oxide powders and thin films were prepared using co-precipitation and traditional mixing methods [52,53] alongside Cu-doped ZnO thin layers deposited via sol–gel techniques on ceramic substrates [33,51], all evaluated for their efficacy in dye degradation through photocatalysis [51–53].

This work presents a systematic review and comparative analysis of our six-year research program (2017–2023) on Algerian kaolinite (DD3)-based photocatalysts. By evaluating four preparation methods (traditional mixing, co-precipitation, sol–gel, and autoclave) and three metal oxides (ZnO, CuO, MgO) under controlled conditions, we identify optimal strategies for photocatalytic applications. Unlike conventional reviews, this analysis leverages internally consistent datasets from our previous studies [33,51–53], all using identical Guelma kaolinite substrates and Orange II dye degradation tests, enabling direct method–performance comparisons.

In this study, we have investigated the application of photocatalysis using ceramic materials, focusing on the role of kaolin as a base catalyst and the impact of added oxides like zinc, copper, and magnesium oxide [54]. We utilized various preparation methods, including dip-coating and autoclave techniques for applying thin layers on ceramic substrates [33,51] and deposition and mixing methods for integrating the oxides [52,53]. The objective was to evaluate the effectiveness of these materials and techniques in enhancing photocatalytic performance for environmental pollutant degradation (Figure 1), thereby contributing to the advancement of sustainable technologies for environmental remediation.

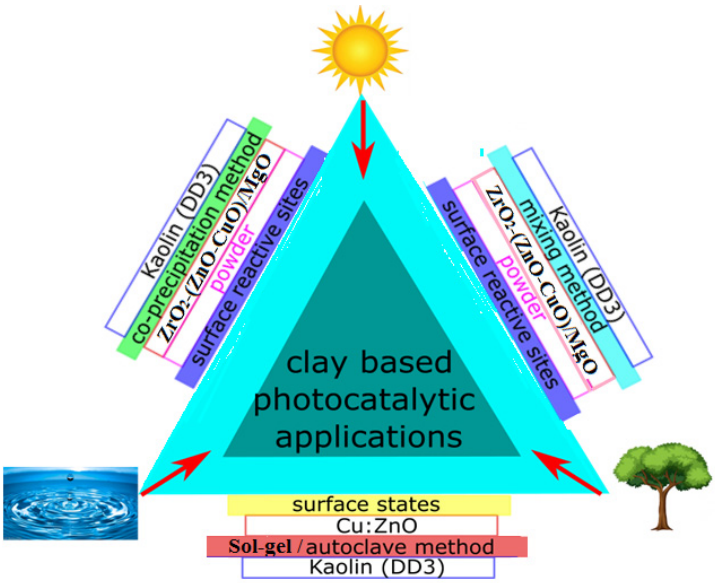


Figure 1. Local kaolin-based material prepared using different methods for photocatalysis.

2. Synthesis and Deferent Preparation Methods

2.1. Prepare Powders DD3 and DD3 + 38 wt.% ZrO_2

The clay materials used in this study, known as DD3 [33], are locally sourced from kaolinitic deposits located in Jebel Debbagh, situated west of Guelma in eastern Algeria (36°31′52 N, 7°16′03 E) [35]. These deposits, dating from the Miocene to the Quaternary periods, are within an ancient collapsed basin, chosen for their accessibility and significance in ceramic and refractory industries [55]. The raw clay materials were processed by wet grinding following initial crushing. Grinding occurred in porcelain jars with agate balls rotating at 200 r/min to prevent contamination [52].

The resulting slip underwent drying at 100 °C, followed by a second grinding to achieve a fine powder, which was subsequently sieved through a 50 µm mesh. Granules of this size were calcined at 560 °C for 6 h to remove moisture and hydrate the halloysite and part of the water from the kaolinite, initiating metakaolin transformation [53]. To reduce residual silica and promote the formation of mullite from kaolinite [52,53], 38% zirconia (ZrO_2) was added to the clay mixture [53]. Heat treatment at 1300 °C for two hours resulted in two distinct powders: mullite and cristobalite for DD3 and mullite and zircon for DD3 + 38 wt.% ZrO_2 [51,54], as depicted in Figure 2.

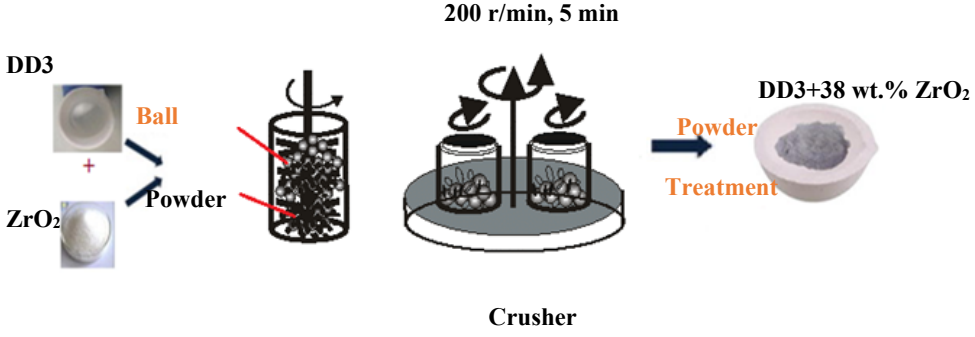


Figure 2. Method used to prepare the DD3 + 38 wt.% ZrO_2 compound.

2.2. Methods Used to Prepare Powders by Adding Oxides (ZnO, CuO, and MgO)

Two methods were employed to prepare the powders, involving traditional mixing [52,53] and co-precipitation techniques [52].

2.2.1. Traditional Milling Method

This approach combined kaolinite powder with mullite-cristobalite (DD3 type) and mullite-zircon (DD3 + 38 wt.% ZrO_2 type) at specific weight ratios: 100 wt.% kaolinite, 69.2 wt.% DD3, and 62.5 wt.% DD3 + 38 wt.% ZrO_2. Zinc oxide (ZnO) was added at varying percentages (0 wt.%, 28 wt.%, and 25 wt.%), while copper oxide (CuO) additions were 0 wt.%, 2.8 wt.%, and 5.37 wt.%, respectively [52]. Additionally, magnesium oxide (MgO) was included at 0 wt.%, 30.8 wt.%, and 37.5 wt.% for the two ceramic compositions [53]. The mixture was homogenized with a small amount of distilled water and blended at 200 rpm for 5 min. Subsequently, the resulting blend was dried in an oven at 200 °C for 15 min (Figure 3), followed by a heat treatment in the same oven at 500°C for two hours, a temperature previously optimized in related studies [52,56,57].

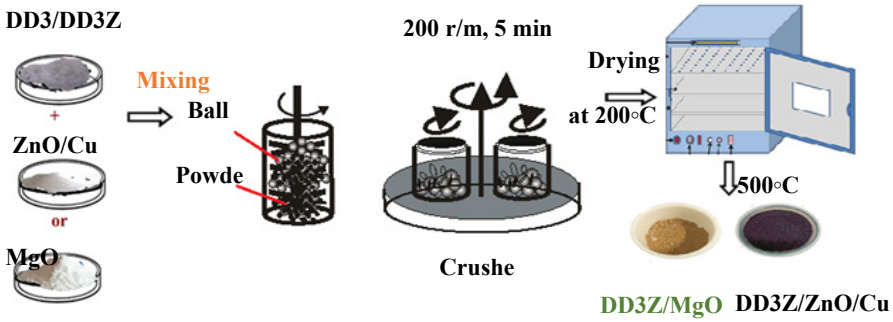


Figure 3. Preparation of DD3Z/ZnO/CuO and DD3Z/MgO using the mixing method.

2.2.2. Co-Precipitation Method

In the co-precipitation method [52] (Figure 4), varying amounts of zinc acetate dihydrate ($(CH_3COO)_2$ $Zn{\cdot}2H_2O$) and copper acetate ($(CH_3COO)_2Cu$) were added to the ceramic materials DD3 and DD3 + 38% ZrO_2-clay. Specifically, zinc acetate was added at 28 wt.% and 25 wt.% for DD3 and DD3 + 38% ZrO_2-clay, respectively, while copper acetate additions were 2.8 wt.% and 12.5 wt.% for the same compositions [52]. The acetates were dissolved in 100 mL of distilled water, followed by adding 3 g of sodium hydroxide (NaOH) to achieve a concentration of 0.5 mol/L in the ceramic and acetate mixture [56,58]. The mixture was stirred at 70 °C for 3 h, causing the formation of metal complex precipitates [59]. The resulting precipitate was filtered under vacuum, washed once with distilled water, and air-dried at 200 °C for 10 min. Subsequently, the dried residue underwent calcination in a Nabertherm oven at 500 °C for 2 h [52,59].

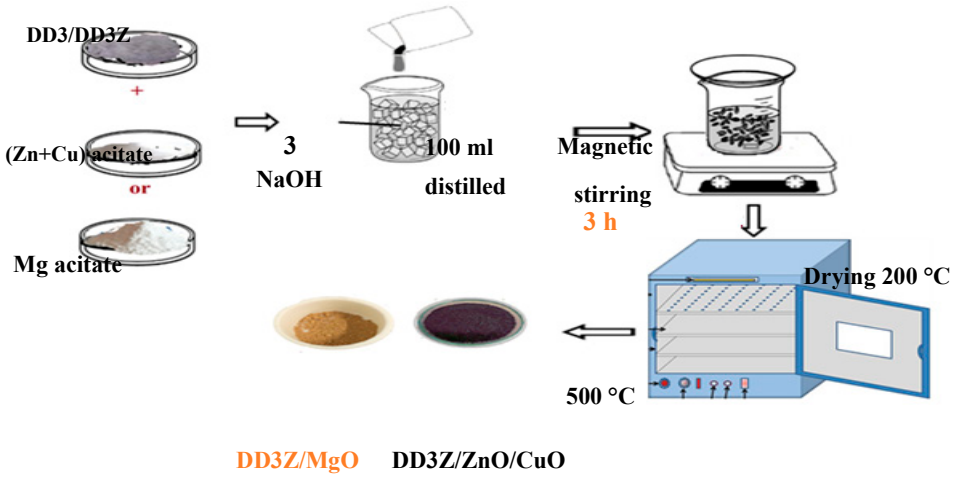


Figure 4. Preparation of DD3Z/ZnO/CuO and DD3Z/MgO using the co-precipitation method.

2.3. Solution Preparation for Sol–Gel and Autoclave Methods

The zinc acetate and copper solutions were prepared in a meticulously cleaned and dried 50 mL beaker and pre-heated to 50 °C, intended for subsequent sol–gel and autoclave methods in sample preparation [33]. For the zinc oxide solution, 3.51 g of zinc acetate dihydrate ($Zn[COOCH]_2 \cdot 2H_2O$), with a molar mass of 219.49 g/mol, was dissolved in 40 mL of absolute ethanol, resulting in a molar concentration of 0.4 mol/L [35]. To incorporate copper into the solution, 6% copper acetate ($Cu(CH_3COO)_2$), equivalent to 0.21 g, was added based on optimal weight ratios observed in powder preparations and converted into a percentage [51]. The solutions were mixed using a magnetic stirrer at approximately 500 rpm for 2 min initially. Subsequently, 2 mL of ethanolamine catalyst (C_2H_7NO) was introduced to the solution, which was maintained on the magnetic stirrer at 70 °C for two hours to facilitate complete mixing and reaction [33,51].

2.3.1. Experimental Steps and Method Used to Form Thin Layers

The samples (Figure 5) were prepared using DD3 clay powders, and 38 wt.% zirconium oxide (ZrO_2) was added [33], achieving a specific open porosity of 33% through controlled heat treatment. Initially, the mass of 1 g of these powders was determined, followed by compacting them into pellets using a "Specac Oum El bouagi-Algeria" press equipped with a 13 mm radius matrix under 40 MPa pressure [35]. Subsequently, the pellets underwent sintering in an oven at 1300 °C for 2 h, with a gradual annealing rate of 5 °C/min (Figure 5) [33,35]. The next step involved depositing active layers of ZnO and Cu-doped ZnO onto these ceramic substrates, which have dimensions of 10.5 mm in diameter and 20 mm in height, utilizing sol–gel and autoclave techniques to enhance their catalytic properties [33,51].

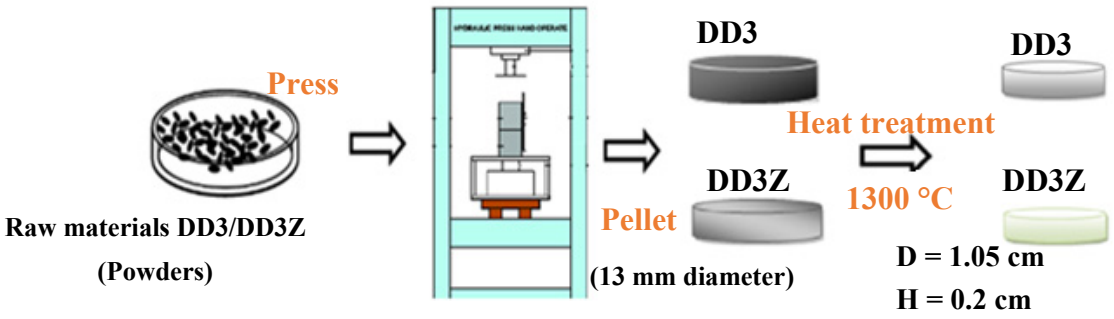


Figure 5. Preparation of substrates from DD3 and DD3 + 38 wt.% ZrO_2.

Sol–Gel Method with Dip-Coating Technique

This technique involves immersing or withdrawing the substrate into/from a gel solution until a thin layer forms on its surface [60]. The solution is heated at 70 °C for 15 min before use. During immersion of the substrate (DD3/DD3 + 38 wt.% ZrO_2) into the gel at 100 mm/min, it remains submerged for one minute before being withdrawn at the same speed [33,35]. The sample is then dried at 200 °C for 3 min in cycles to remove various compounds such as solvents, water, and impurities from the gel sediment. This dipping and drying process is repeated 50 times to achieve thin layers deposited on both sides of the ceramic substrate [61]. Finally, the samples undergo heat treatment at 500 °C for 2 h (Figure 6) [33,35].

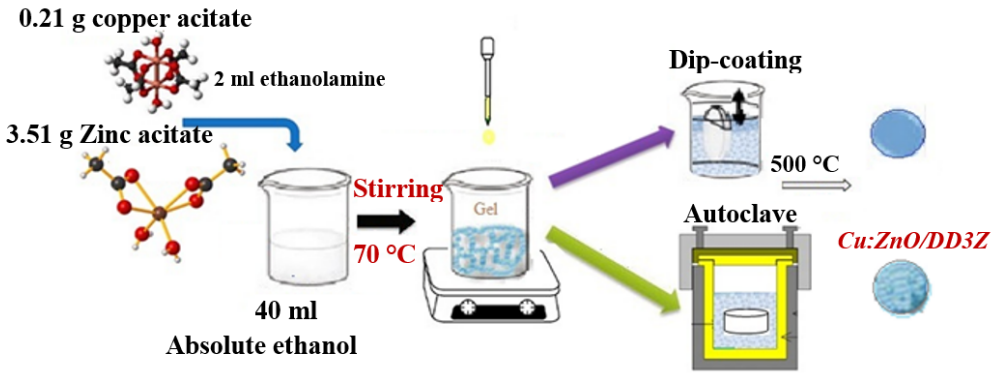


Figure 6. Deposition of Cu:ZnO thin layers on ceramic substrates.

Autoclave Method

The same solution was prepared using the method above and applied to ceramic samples of the same type (DD3/DD3 + 38 wt.% ZrO_2) using the autoclave technique [51]. Initially, 10 mL of the prepared solution was placed in a Teflon container, which was then securely sealed and positioned in an oven at 300 °C [51]. After 75 min, a deposited layer formed on the substrate surface. Subsequently, the sample underwent drying at 200 °C for 5 min, followed by curing at 500 °C for 2 h to achieve a crystalline surface (Figure 6) [51,62].

The Table 1 summarizes the various materials, preparation methods, conditions, and sources mentioned in the document. It provides a clear overview of the different experimental procedures used in the study [33,51–53].

Table 1. Summarizing the different materials, preparation methods, conditions, and sources [33,35,51–53].

Material	Preparation Method	Conditions	Source	Ref.
DD3	Wet grinding, drying, calcination	- Wet grinding at 200 r/min - Drying at 100 °C - Sieving through 50 µm mesh - Calcination at 560 °C for 6 h - Heat treatment at 1300 °C for 2 s	Jebel Debbagh, Algeria	[51]
DD3 + 38 wt.% ZrO_2	Same as DD3, with ZrO_2 addition	Same as DD3	Jebel Debbagh, Algeria + ZrO_2 addition	[51]
DD3Z/ZnO/CuO	Traditional mixing	- Mixing at 200 rpm for 5 min - Drying at 200 °C for 15 min - Heat treatment at 500 °C for 2 h	DD3 + ZnO + CuO	[51]
DD3Z/MgO	Traditional mixing	Same as DD3Z/ZnO/CuO	DD3 + MgO	[51]
DD3Z/ZnO/CuO	Co-precipitation	- Stirring at 70 °C for 3 h - Drying at 200 °C for 10 min - Calcination at 500 °C for 2 h	DD3 + zinc acetate + copperacetate	[52]
DD3Z/MgO	Co-precipitation	Same as DD3Z/ZnO/CuO (co-precipitation)	DD3 + magnesium oxide	[53]
ZnO solution	Sol–gel	- Mixing at 500 rpm for 2 min - Stirring at 70 °C for 2 h	Zinc acetatedihydrate + ethanol + ethanolamine	[33]
Cu-doped ZnO solution	Sol–gel	Same as the ZnO solution	Zinc acetatedihydrate + copperacetate + ethanol + ethanolamine	[33]

Table 1. *Cont.*

Material	Preparation Method	Conditions	Source	Ref.
ZnO thin layers	Sol–gel (dip-coating)	- Dipping speed: 100 mm/min - Drying at 200 °C for 3 min (50 cycles) - Heat treatment at 500 °C for 2 h	ZnO solution + DD3 or DD3 + 38 wt.% ZrO_2 substrate	[33]
Cu-doped ZnO thin layers	Sol–gel (dip-coating)	Same as ZnO thin layers	Cu-doped ZnO solution + DD3 or DD3 + 38 wt.% ZrO_2 substrate	[33]
ZnO thin layers	Autoclave	- 300 °C for 75 min - Drying at 200 °C for 5 min - Curing at 500 °C for 2 h	ZnO solution + DD3 or DD3 + 38 wt.% ZrO_2 substrate	[51]
Cu-doped ZnO thin layers	Autoclave	Same as ZnO thin layers (autoclave)	Cu-doped ZnO solution + DD3 or DD3 + 38 wt.% ZrO_2 substrate	[51]

2.4. Photocatalytic Testing

The photocatalytic efficacy of the synthesized catalyst materials was evaluated by measuring the degradation of an Orange II dye solution. We selected Orange II dye as a benchmark pollutant because it enables direct comparison with our previous studies and provides rapid screening of photocatalytic activity. While this approach has known limitations regarding environmental relevance, it offers reproducible, quantitative data for method development.

All reactions were conducted in a cylindrical Pyrex glass reactor (5 cm diameter, 150 mL volume) with a water-cooled quartz jacket. We opted for an open-top design to permit natural oxygen exchange (critical for ROS generation), with the 300 W xenon lamp fixed 10 cm above the solution surface. Magnetic stirring at 500 rpm maintained suspension, though some powder accumulation occurred near the walls after prolonged runs—a known limitation of this configuration.

Solutions containing 25 mg/L of the dye for ceramic powders and 12.5 mg/L for ceramic slice samples were prepared. Ceramic slice samples coated with Cu-doped ZnO layers and 0.1 g of ceramic powders with varying proportions of ZnO-CuO/MgO were dispersed in 25 mL of the aqueous dye solution. For the ceramic slice samples, the suspensions were stirred under dark conditions for 30 min to establish adsorption–desorption equilibrium before being exposed to a 300 W xenon lamp with a UV cutoff filter ($\lambda > 400$ nm) at room temperature for 4 h. The 30 min stirring time under dark conditions was selected based on preliminary tests. UV-Vis spectrophotometry monitored the Orange II concentration overtime during these preliminary tests. It was observed that after 30 min of stirring in the dark, the dye concentration stabilized, confirming the establishment of adsorption–desorption equilibrium. No further significant decrease in absorbance was recorded beyond this point. Thus, 30 min was chosen as the optimal duration to ensure reliable photocatalytic activity measurements.The reaction mixture (Figure 7) was maintained at 25 °C using a circulating water bath throughout irradiation, and light intensity was controlled at 100 mW/cm^2. Every hour, 2 mL aliquots were withdrawn and analyzed by UV-Vis spectrophotometry (Shimadzu UV-2600i from MOLTECH Angers, France) in the 250–650 nm wavelength range to monitor dye concentration changes. For the ceramic powder suspensions, the setup remained similar. Samples were collected every 20 min, centrifuged at 4000 rpm for 5 min to separate the catalyst, and then analyzed using UV-Vis spectrophotometry. Degradation efficiency was calculated by tracking the decrease in absorbance at 484 nm, the maximum absorption peak of Orange II. Control experiments

were performed without the catalyst to verify that the dye degradation was due to photocatalytic activity and not photolysis. For ceramic slice samples tested under the 300 W xenon lamp, Orange II solutions without catalysts showed less than 3% degradation after 6 h. No significant decrease in dye concentration was observed during irradiation for powder samples tested under visible light. These results confirm that photolysis under the applied conditions was negligible and that the observed degradation is primarily due to the photocatalytic action of the synthesized materials.The choice of Orange II as a model pollutant reflects its frequent use in photocatalytic performance studies alongside other compounds like methylene blue, Rhodamine B, and tetracycline hydrochloride. Although UV-Vis spectroscopy served as the primary analytical tool in this study, advanced techniques like total organic carbon (TOC) analysis and high-performance liquid chromatography (HPLC) are often applied in similar work to provide deeper insight into mineralization processes.



Figure 7. The method used to prepare Orange II solutions for the photocatalysis experiment.

3. Discussion

3.1. Structural Characterization

3.1.1. X-Ray Diffraction

Samples prepared using various fabrication methods exist in either powder or ceramic slice forms, with or without the addition of ZrO_2 [33,51–53]. Subsequently treated at 500 °C, these samples undergo X-ray diffraction (XRD) analysis. Figure 8 illustrates the characterization of these samples under the permission of [33,35,51–53]. The predominant phases identified in the ceramics include mullite (JCPDS 15-0776) and cristobalite (JCPDS 01-0424) for DD3-clay-based substrates and zircon (JCPDS 06-0266) and zirconia (JCPDS 37-1484) for DD3 + ZrO_2-based substrates [33,35].

By employing co-precipitation and mixing techniques and incorporating zinc and copper oxides [52], it was noted that all spectra exhibit distinct intensity peaks corresponding to Wurtzite-type ZnO (JCPDS 36-1451) [63,64], particularly notable at a 50 wt.%ZnO content [52]. Upon the addition of MgO, a singular low-intensity peak corresponding to the MgO phase, specifically at the (200) level, becomes apparent [53]. The observed spectral shifts indicate structural distortion due to the expansion of the unit cell dimensions, attributed to the introduction of atoms into vacant sites (Mg^{2+} = 0.72 Å, Cu^{2+} = 0.73 Å, Zn^{2+} = 0.74 Å) within the kaolin-based ceramic matrix (Al^{3+} = 0.5 Å, Si^{4+} = 0.40 Å) [52,53]. The results demonstrate that the co-precipitation method yields finer particles [52].

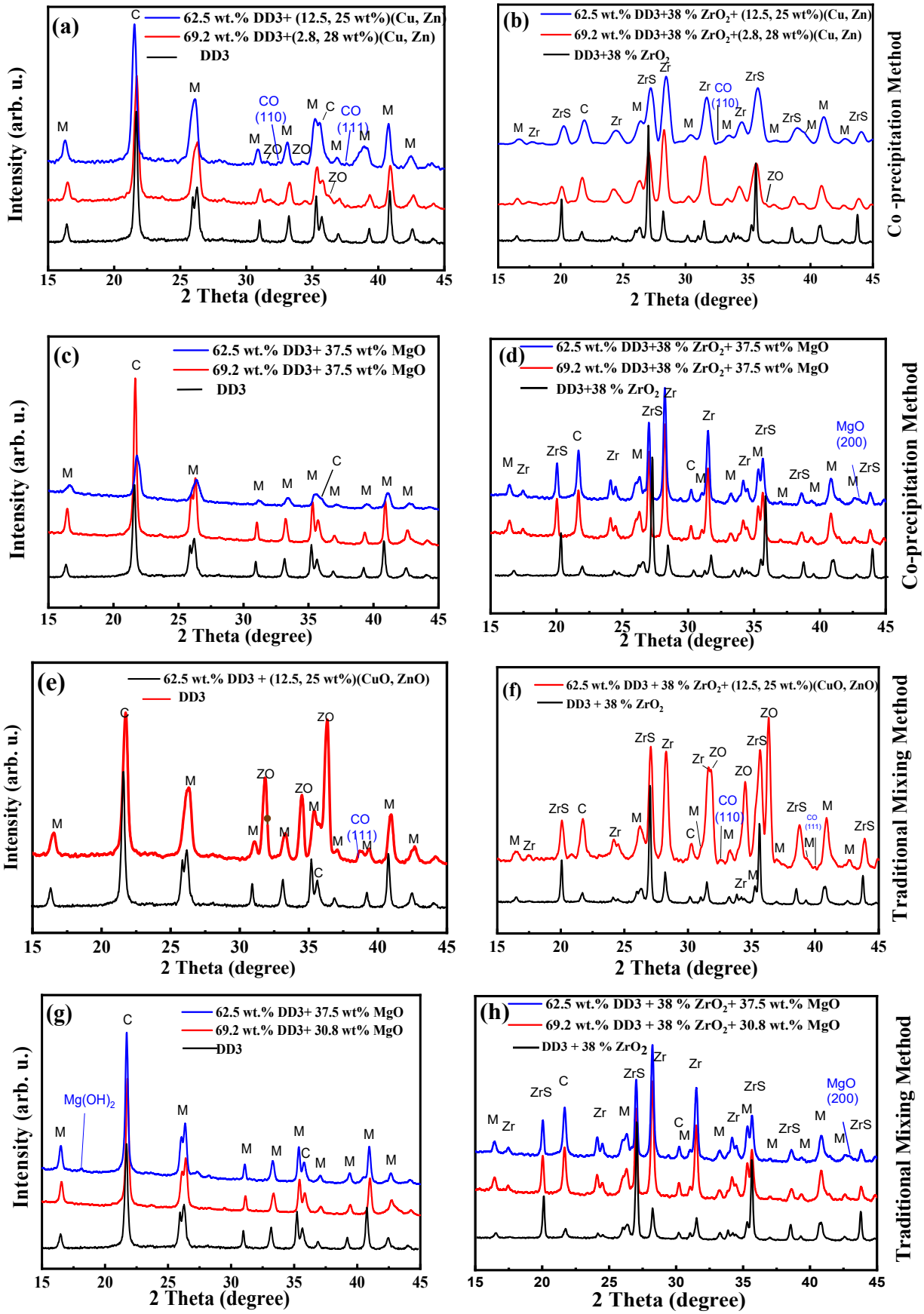


Figure 8. XRD spectra of ceramic powders. Reprinted with permission of [52,53]. ZrS: zircon ($ZrSiO_4$), Zr: zirconia (ZrO_2), C: cristobalite (SiO_2), M: mullite ($3Al_2O_3$, $2SiO_2$). (**a**–**d**) Co-precipitation method, (**e**–**h**) traditional mixing method.

The comparison between precipitation and mixing techniques for adding oxides to DD3 and DD3 + ZrO_2 substrates reveals that both methods successfully incorporate ZnO, CuO, and MgO into the ceramic matrix [52,53], as evidenced by the appearance of Wurtzite-type ZnO peaks in XRD spectra. However, the co-precipitation method yields finer particles, potentially leading to better dispersion and enhanced properties [65]. The observed spectral shifts, both to the right and left, are attributed to structural distortions in the crystal lattice [52,53]. Shifts to lower angles (left) typically indicate an expansion of the unit cell, often caused by the incorporation of larger ions (Mg^{2+}, Cu^{2+}, Zn^{2+}) into the kaolin-based ceramic matrix (containing smaller Al^{3+} and Si^{4+} ions) [52,53].

Conversely, shifts to a higher angle (right) may suggest lattice contraction, possibly due to the creation of oxygen vacancies or other defects during the doping process [66]. These shifts are consistent with Vegard's law, which describes how lattice parameters change with composition in solid solutions [67]. The direction and magnitude of these shifts provide valuable insights into the nature of the dopant incorporation and its effects on the crystal structure, which can significantly influence the material's physical and chemical properties [68].

Our research findings show strong alignment with the existing literature across several dimensions, particularly in terms of the effects of preparation methods on particle size and the influence of doping on crystal structure [69]. Using ceramic substrates (DD3 and DD3 + ZrO_2) adds a unique aspect to this study, potentially offering new insights into the growth and properties of ZnO and doped ZnO materials on complex ceramic surfaces [52–54].

Recent studies have further elucidated the relationship between synthesis methods and photocatalytic performance. Lim et al. [70] demonstrated that optimized precipitation methods yield ZnO nanoparticles with enhanced crystallinity and visible-light activity, corroborating our findings of finer particle formation through co-precipitation. Alasmari et al. [71] showed that rare-earth doping (Gd) in ZnO nanocomposites improves phase purity and photocatalytic efficiency, aligning with our observations of structural modifications via metal oxide incorporation. The doping-induced peak shifts in our XRD analysis find strong support in the work of El-Sayed et al. [72], who documented similar lattice distortions in Nd_2O_3-doped CuO systems. Atta et al. [73] provided additional validation through their detailed characterization of sol–gel-derived ZnO thin films, confirming the method-dependent control over crystallite size and orientation that we observed. Most recently, Mosleh et al. [74] systematically investigated Ag-doped CuO nanoparticles, demonstrating how dopant integration affects structural properties and photocatalytic performance.This finding parallels our results with mixed oxide systems. These contemporary studies collectively reinforce our methodological approach while highlighting advancements in the field since the earlier works cited in our original manuscript [52,53]. In conclusion, our study corroborates previous research on the impact of preparation methods and doping on ZnO properties while contributing new insights into the behavior of ZnO and doped ZnO materials on complex ceramic substrates [52,53].

Thin layers of Cu/DD3 and Cu/DDZ are fabricated using the sol–gel [33] and autoclave [51] methods (Figure 9). The X-ray diffraction (XRD) patterns reveal prominent peaks corresponding to zinc in two phases (JCPDS 03-0891) oriented preferentially at (100), (002), and (101) [75] and copper oxide (JCPDS 01-1117) with orientations (11-1) and (111) when using the autoclave method [76]. During the dip-coating process, the substrate's pores are filled with Cu-doped ZnO [33], and subsequent rearrangement of the deposited crystals induces compressive stress and XRD peaks towards larger angles [33].

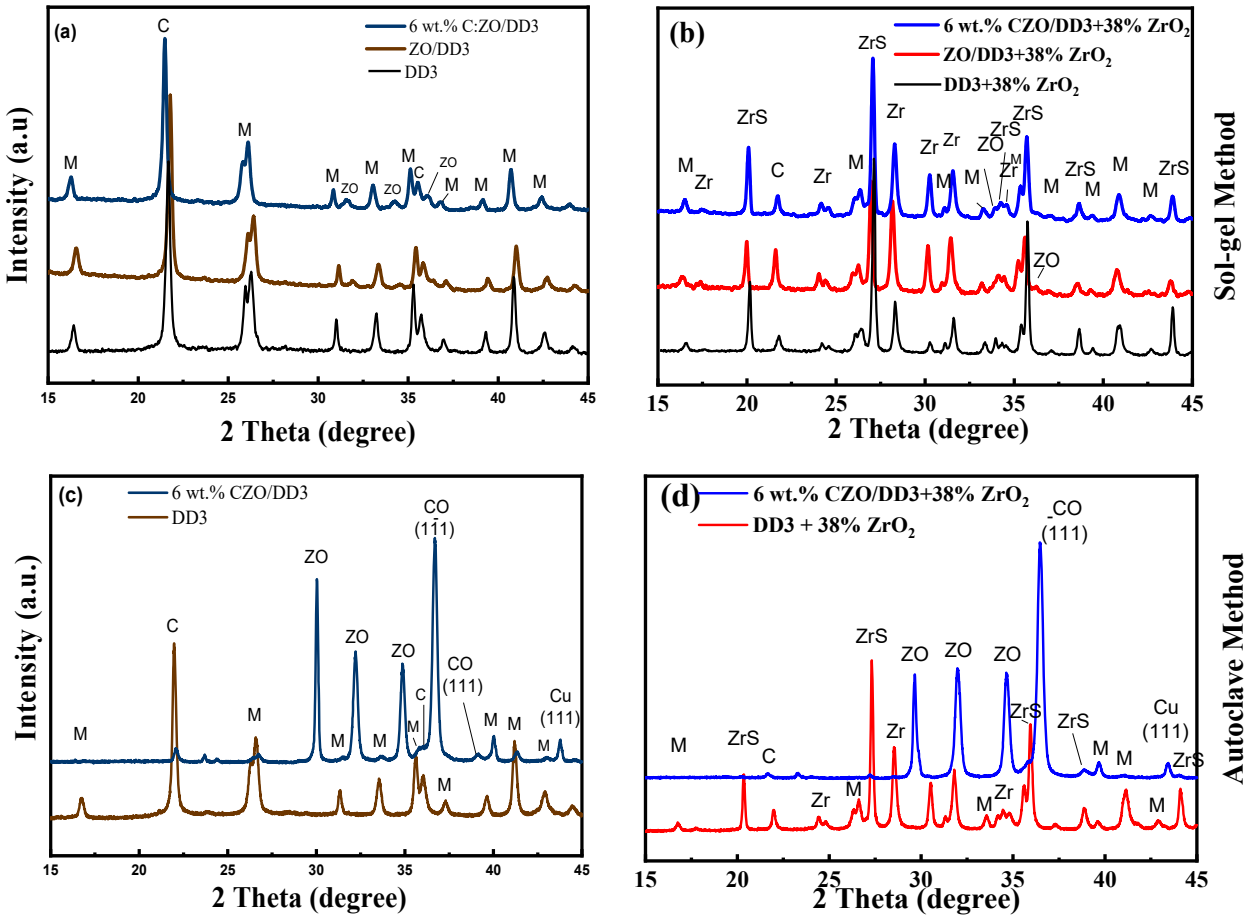


Figure 9. XRD spectra of Cu: ZnO thin layers deposited on different substrates prepared by sol–gel and autoclave methods before and after doping. Reprinted/adapted with permission of [33,51]. (**a**,**b**) Sol–gel method. (**c**,**d**) Autoclave method.

The comparison between the sol–gel (dip-coating) and autoclave methods for depositing Cu-doped ZnO thin layers on DD3 and DDZ substrates reveals distinct differences in crystalline structure and orientation [33,51]. The autoclave method produces more prominent peaks for zinc and copper oxide phases, with preferential orientations at (100), (002), and (101) for zinc and (11-1) and (111) for copper oxide [51]. In contrast, the sol–gel method produces less pronounced peaks, suggesting smaller crystallite sizes or a more amorphous structure [33].

The doping process in both methods leads to spectral shifts, with the sol–gel method showing a tendency for peaks to shift towards larger angles due to compressive stress induced by crystal rearrangement within substrate pores [33]. These shifts can be explained by Bragg's law ($n\lambda = 2d \sin \theta$), where a decrease in interplanar spacing (d) due to compressive stress results in an increase in the diffraction angle (θ) [77]. Conversely, shifts to lower angles may occur due to tensile stress or the incorporation of larger Cu^{2+} ions (0.73 Å) into the ZnO lattice (Zn^{2+} = 0.74 Å), causing lattice expansion [78].

These observations (Table 2) align with research by Wang et al. [79], who reported similar peak shifts in Cu-doped ZnO nanostructures prepared by various methods [79]. Additionally, the work of Muchuweni et al. [80] on sol–gel-derived Cu-doped ZnO thin films corroborates our findings on the relationship between doping concentration and peak shifting. The differences in crystallinity and orientation between the two methods highlight the significant impact of the preparation technique on the final material properties

(Table 2), consistent with the findings of Lim et al. [70] in their comparative study of ZnO nanoparticle synthesis methods.

Table 2. Comparison of X-ray analysis results with previous studies.

Current Study	Previous Research	Comparison	Ref.
Wurtzite-type ZnO peaks observed in both mixing and precipitation methods	Lim et al. (2024): Recent modifications in ZnO photocatalysts for dye degradation	Confirms ZnO crystallinity and its role in photocatalytic activity under visible light	[70]
Co-precipitation method yields finer particles	Alasmari et al. (2024): Gd-doped ZnO nanocomposites with enhanced degradation performance	Highlights the advantage of co-precipitation for particle size control and doping efficacy	[71]
Spectral shifts due to dopant incorporation (Cu, Mg)	El-Sayed et al. (2022): Nd_2O_3-doped CuO NPs for methylene blue degradation	Demonstrates successful dopant integration and lattice distortion effects	[72]
Substrate composition (DD3 vs. DD3 + ZrO_2) influences ZnO growth	Atta et al. (2024): Sol–gel ZnO thin films for MB degradation	Corroborates substrate-dependent photocatalytic performance	[73]
Sol–gel method shows peak shifts due to compressive stress	Mosleh et al. (2024): Ag-doped CuO NPs for antimicrobial and photocatalytic applications	Supports method-dependent structural modifications	[74]

3.1.2. Scanning Electron Microscopy (SEM) and Transmission Electron Microscopy (TEM)

The shape and size of sample grains prepared using different ceramic materials and metal-oxide additives were examined using SEM and TEM [52,53]. SEM analysis of the catalyst materials, produced via the traditional mixing method using ceramic/MgO [53] and ceramic/ZnO-CuO [52] powders, revealed significant morphological changes. Specifically, Figure 10 illustrates a notable transformation in grain shape upon adding zirconium oxide to DD3, accompanied by an increase in porosity from 50.2 nm to 292.5 nm [52]. This transformation highlights the impact of zirconium oxide on grain structure, leading to increased porosity [54]. TEM analysis further confirmed these observations, revealing well-dispersed nanoparticles with an average size of ~50 nm, consistent with the SEM findings. The high-resolution TEM (HR-TEM) images showed distinct lattice fringes corresponding to the ZnO, CuO, and MgOcrystalline phases, confirming their successful integration into the ceramic matrix.

Further addition of zinc and copper oxides to both ceramic types significantly enhanced pore formation [52], as evidenced by SEM and TEM. The flake-like structure of DD3Z, compared to DD3, was visible in SEM (Figure 10b), while TEM provided additional insight into the nanoscale porosity and particle distribution [52]. Similarly, incorporating magnesium oxide into DD3 + ZrO_2 resulted in greater porosity than unmodified DD3 [53], with TEM images revealing a more uniform distribution of MgO nanoparticles within the ceramic framework. The combined SEM and TEM analyses demonstrated that the inclusion of zinc, copper, and magnesium oxides markedly increases the porous structure, making these materials highly suitable for photocatalytic applications by enhancing impurity capture from pollutant dye solutions [52,53].

Figure 10 showcases SEM images of ceramic powders prepared by traditional mixing with the addition of ZnO, CuO, and MgO. Specifically, Figure 10a depicts the pure DD3 ceramic with irregular, flake-like particles. In contrast, Figure 10b displays DD3 + 38 wt.% ZrO_2, revealing a denser structure with smaller, more uniform particles due to ZrO_2 addition [52]. TEM analysis of these samples confirmed the reduced particle size and

improved homogeneity, with no large agglomerates observed. Figure 10c,d demonstrate the effects of adding ZnO and CuO to DD3 and DD3 + ZrO_2, respectively, showing agglomerated structures with increased porosity in SEM [52], while TEM highlighted the interfacial contact between the metal oxides and the ceramic substrate, which is critical for charge transfer in photocatalysis. Furthermore, Figure 10f illustrates the impact of MgO addition, resulting in larger, more rounded particles with a smoother surface in SEM [53]. At the same time, TEM revealed that these particles maintained a high degree of crystallinity, further supporting their stability under photocatalytic conditions.

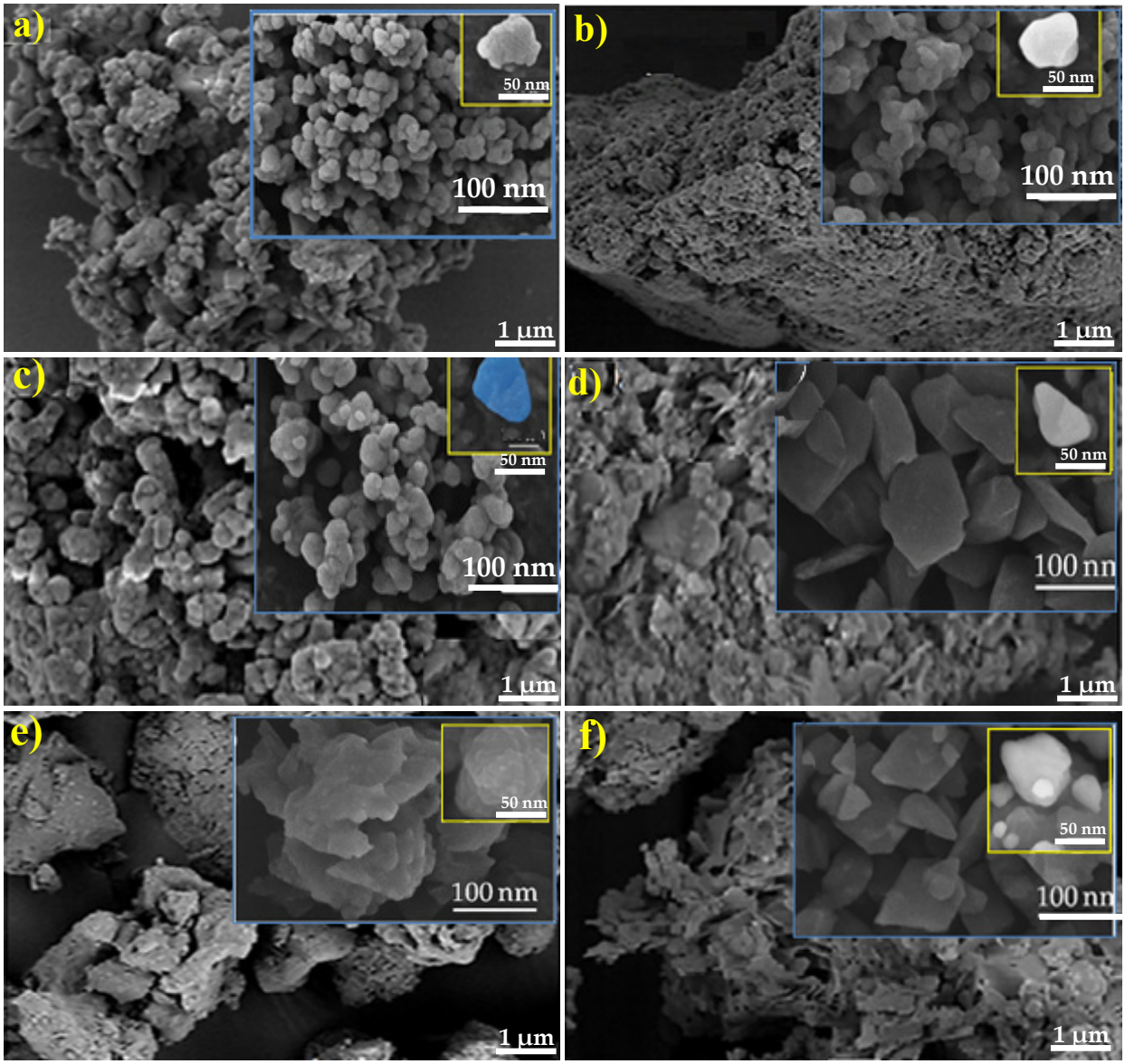


Figure 10. SEM and TEM images of powder ceramics prepared by traditional mixing with the addition of ZnO, CuO, and MgO. Reproduced with permission [52,53]. DD3 (**a**), DD3 + 38 wt.% ZrO_2 (**b**), DD3/28 wt.% ZnO/2.8 wt.% CuO (**c**), DD3 + 38 wt.% ZrO_2/28 wt.% ZnO/2.8 wt.% CuO (**d**), DD3/30.8 wt.% MgO (**e**), and DD3 + 38 wt.% ZrO_2/30.8 wt.% MgO (**f**).

Recent studies have provided valuable insights that corroborate our morphological observations. Quy et al. [81] demonstrated that chitosan/ZnO-Fe_3O_4 nanocomposites exhibit similar structural heterogeneity when prepared through mixing methods, particularly noting the relationship between particle size distribution and photocatalytic efficiency. Their findings using advanced characterization techniques align closely with our results

regarding the impact of preparation methods on material morphology. Furthermore, Saha et al. [82] systematically investigated CuO nanoparticles for RhB dye degradation, revealing howparticle shape and size distribution variations affect photocatalytic performance—a relationship we similarly observed in our mixed oxide systems. These contemporary studies collectively reinforce our understanding of how synthesis techniques influence the structural properties of ceramic photocatalysts.

Figure 11 presents SEM images of Cu-doped ZnO (CZO) thin layers deposited on different substrates using sol–gel and autoclave methods [33,51], highlighting distinct morphologies between the two fabrication methods. The sol–gel method results in a predominant flower-like growth pattern with increased surface roughness [33,35], thereby offering a broader active surface area. In contrast, the autoclave method produces thin films characterized by spherical-shaped nanoparticles on the substrate surface [51].

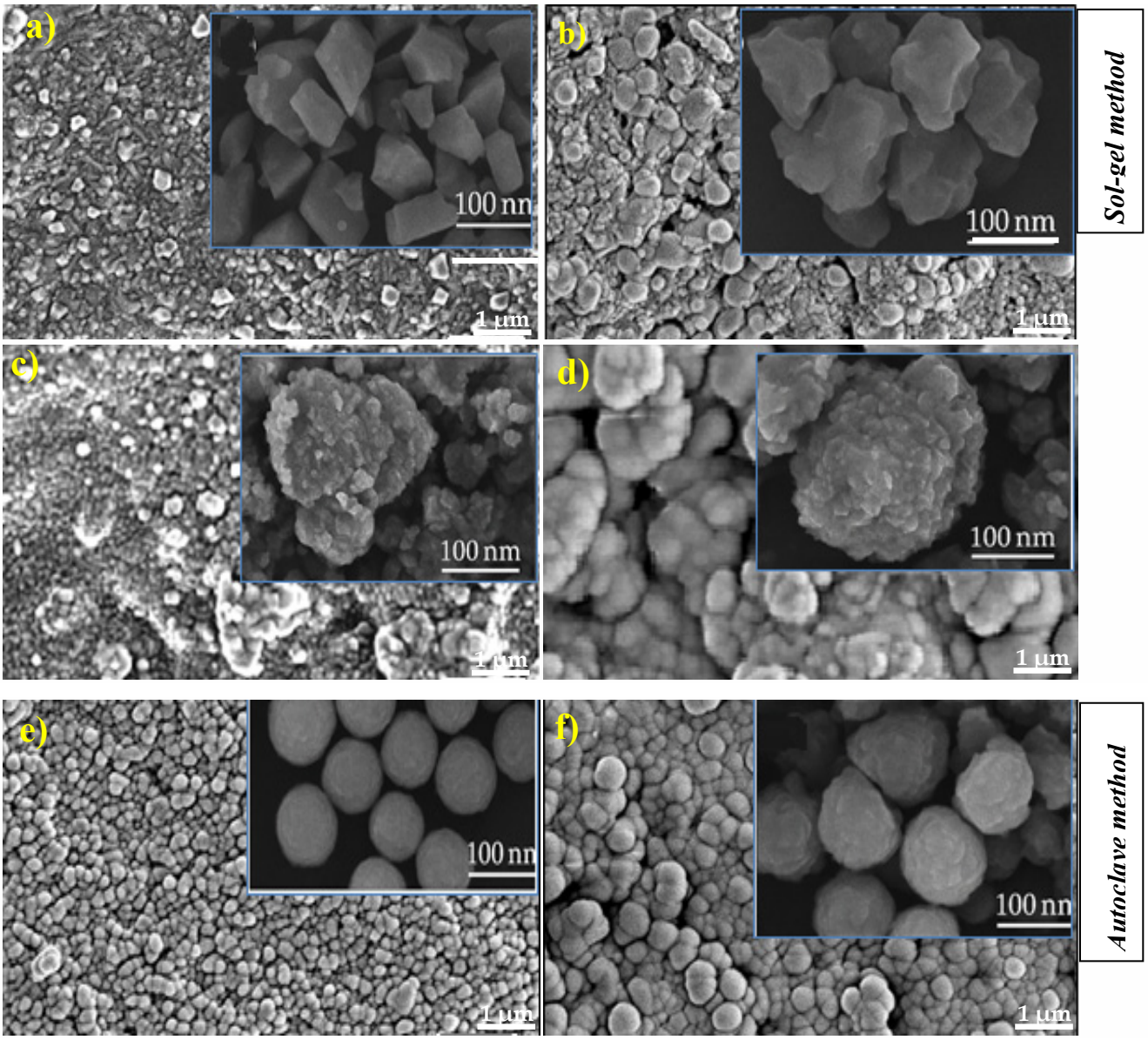


Figure 11. SEM images of thin layers of Cu-doped ZnO (CZO) deposited on different substrates prepared by sol–gel and autoclave methods. Reprinted/adapted with permission of [33,51]. Pure DD3 (**a**), DD3 + 38 wt.% ZrO_2 (**b**), CZO/DD3 (**c**,**e**), CZO/DD3 + 38 wt.% ZrO_2 (**d**,**f**).

Figure 11a,b show the pure DD3 and DD3 + 38 wt.% ZrO_2 substrates, respectively, with (b) displaying a denser, more uniform surface. Figure 11c,e depict CZO layers on DD3 prepared by sol–gel and autoclave methods [33,51]. The sol–gel method (c) produces a more uniform, finer-grained surface than the autoclave method (e), showing larger, more distinct crystallites. Similarly, Figure 11d,f show CZO layers on DD3 + ZrO_2 [33], with the sol–gel method (d) again yielding a smoother, more homogeneous surface than the autoclave method (Figure 11f) [51]. Recent studies have provided valuable insights into the morphological characteristics of photocatalysts prepared through different methods. Aroob et al. [83] demonstrated that green-synthesized CuO nanoparticles exhibit well-defined surface structures with optimal photocatalytic activity, consistent with our observations of uniform morphology in sol–gel-derived samples. The autoclave method's tendency to produce larger crystallites finds strong support in the work of Ahmadpour et al. [84], who systematically investigated substrate surface treatment effects on hydrothermal ZnO nanostructure formation. Their findings on the relationship between synthesis parameters and particle morphology directly corroborate our results regarding preparation method-dependent surface characteristics. Table 3 provides a concise comparison between these contemporary findings and our current study, highlighting methodological consistencies and novel advancements in understanding how preparation techniques influence ceramic photocatalyst properties.

Table 3. Comparison of SEM results with previous studies.

Current Study	Previous Research	Comparison	Ref.
Traditional mixing produces heterogeneous structures	Quy et al. (2025): Chitosan/ZnO-Fe_3O_4 nanocomposites for dye degradation	Similar observations on composite morphology and pollutant capture efficiency	[81]
Addition of ZnO and CuO increases porosity	Saha et al. (2024): CuO NPs for RhB dye degradation	Confirms porosity enhancement via metal oxide addition	[82]
Sol–gel method yields uniform, fine-grained surfaces	Aroob et al. (2023): Green-synthesized CuO NPs for dye degradation	Aligns with findings on surface uniformity and photocatalytic efficiency	[83]
The autoclavemethod resulted in larger, more distinct crystallites	Ahmadpour et al. (2022)—Larger crystals in the hydrothermal synthesis of ZnO nanostructures	Consistent resultsshowthe tendency of autoclave methods to produce larger crystallites	[84]
Autoclave method results in larger crystallites	Dursun et al. (2020): CuO-WO_3 hybrids for adsorption/photocatalysis	Consistent with hydrothermal synthesis trends	[85]

3.2. EnergyDispersive X-Ray Spectroscopy (EDX)

Elemental analysis using Energy Dispersive X-ray Spectroscopy (EDX) was employed to determine the atomic percentages of key elements (O, Al, Si, Zr, Zn, Mg, Cu) present in various samples [52,53]. The EDX system utilized an electron beam to characterize both the deposited layers and parts of the substrate, as well as the elements within the prepared powders (Figure 12) [52,53]. To ensure treatment homogeneity, multiple spectra were recorded across different regions of the samples on various substrates [52,53]. The average percentages of these main chemical elements are compiled in Table 4.

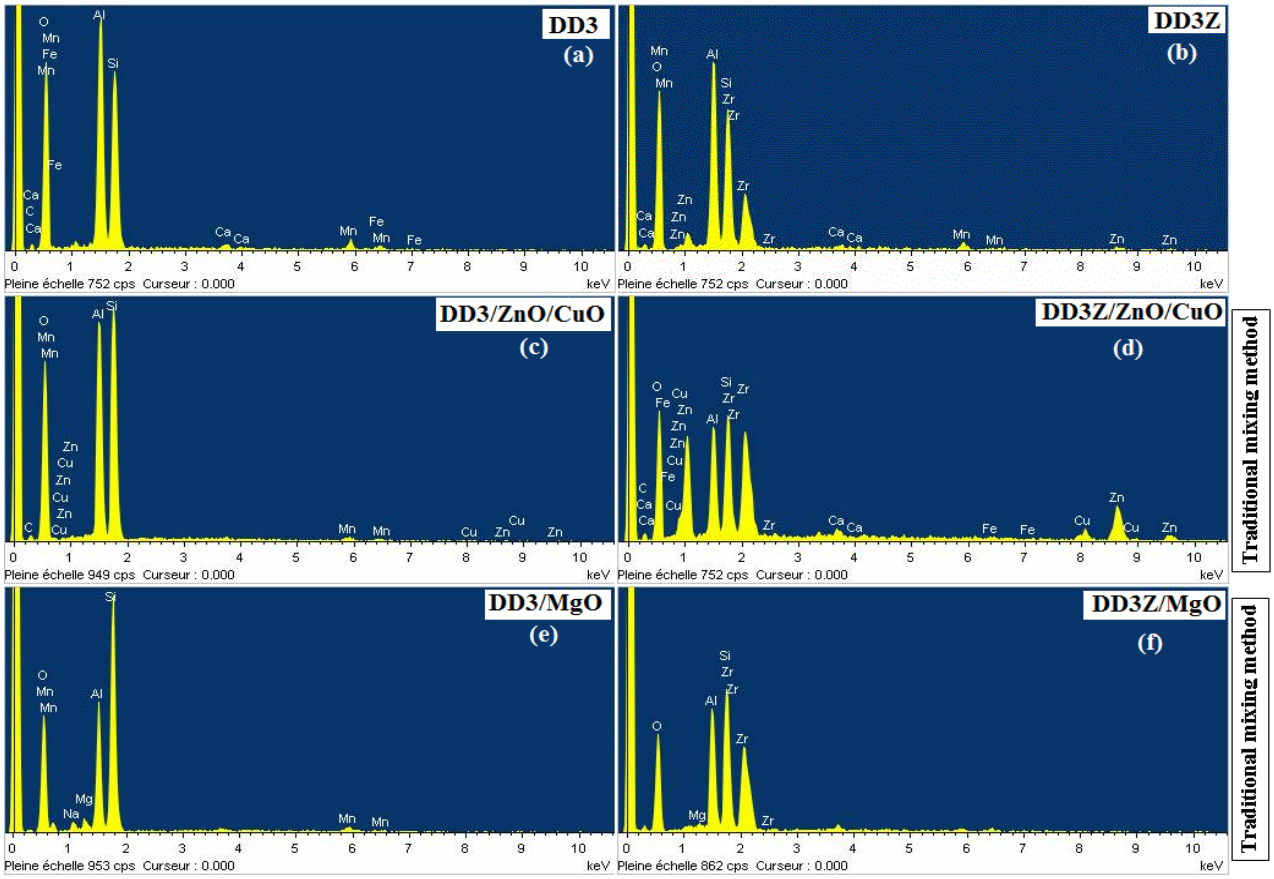


Figure 12. EDS spectrum of ceramic powder after the addition of ZnO, CuO, and MgO. Reprinted/adapted with permission of [52,53]. (**a**) DD3, (**b**) DD3 + ZrO_2, (**c**) DD3/28 wt.% ZnO/2.8 wt.% CuO, (**d**) DD3Z/28 wt.% ZnO/2.8 wt.% CuO, (**e**) DD3/30.8 wt.% MgO, and (**f**) DD3 + ZrO_2/30.8 wt.% MgO.

Table 4. Quantitative analysis of the EDX spectra of the powders prepared by the mixing method [52,53].

Powder	Elements, at.%							
	O (%)	Al (%)	Si (%)	Zr (%)	Mg (%)	Zn (%)	Cu (%)	Mn(%)
DD3	63.35	14.8	13.99	-	-	-	-	4.23
DD3Z	61.93	14.51	12.29	4.24	-	-	-	2.81
DD3/ZnO/CuO	60.36	11.08	14.52	-	-	0.13	0.08	0.36
DD3Z/ZnO/CuO	54.06	7.06	7.17	5.24	-	7.41	1.49	0.25
DD3/MgO	62.61	10.83	23.71	-	0.97	-	-	0.58
DD3Z/MgO	70.72	10	13.62	5.75	0.09	-	-	-

The results confirm that the chemical compositions derived from the samples and the different powders closely align with the expected percentages of the chemical elements introduced during their preparation. Specifically, when ceramics are used as powders, the proportions of essential elements and impurities (Si, Al, Zr, Mg, Cu, Zn) are discernible [52,53]. This characterization underscores the thoroughness of EDX in verifying the elemental uniformity across the treated materials and substrates [33,51–53].

Table 4 shows the chemical composition of various powder samples prepared by the mixing method [52,53]. The base DD3 sample contains 63.35% O, 14.8% Al, 13.99% Si, and 4.23% Mn. When ZrO_2 is added (DD3Z), we see 4.24% Zr appear, while O decreases slightly

to 61.93%. Adding ZnO and CuO (DD3/ZnO/CuO) introduces 0.13% Zn and 0.08% Cu while reducing Mn to 0.36%. In DD3Z/ZnO/CuO, Zn increases to 7.41% and Cu to 1.49%, with Zr at 5.24%, showing a significant incorporation of these elements [52].

Adding MgO (Table 5) (DD3/MgO) introduces 0.97% Mg and increases Si to 23.71%, while in DD3Z/MgO [53], Mg is only 0.09%, but Zr is 5.75%. These changes demonstrate how the mixing method alters the ceramic composition, with some elements being incorporated more effectively than others [53]. When ceramics are used as a substrate [33,51], the predominant elements are typically silicon (Si), aluminum (Al), and zirconium (Zr). After depositing metal-oxide thin layers, such as zinc (Zn) and copper (Cu), these elements appear in small proportions [33,51]. Specifically, copper is detected in very low amounts when prepared using the sol–gel method (Figure 13) [33]. However, when employing the autoclave method, there is a notable absence of substrate elements, with high percentages of sedimentation elements like Zn and Cu observed instead. This discrepancy is attributed to the thickness of the deposited layers [51], which effectively masks the ceramic substrate [51]. It confirms the intentional doping of zinc oxide layers with copper, emphasizing the active role of these elements in the deposited layers. The table compares samples prepared by dip-coating and autoclave methods [33,51].

The base DD3 sample shows 72.79% O, 13.82% Al, and 13.39% Si. When CZO is added (CZO-DD3), we see the introduction of 0.86% Zn and 0.11% Cu, with O increasing to 79.56%, while Al and Si decrease to 10.09% and 9.39%, respectively. Adding ZrO_2 (DD3 + ZrO_2) introduces 6.45% Zr, slightly reducing other elements [33]. The combination of CZO and ZrO_2 (CZO-DD3 + ZrO_2) shows 7.96% Zr, 1.96% Zn, and 0.13% Cu, demonstrating the successful incorporation of all added elements [33]. Interestingly, the lower portion of the table shows dramatically different compositions for CZO-DD3 and CZO-DD3 + ZrO_2, with much higher Zn (47.34% and 38.20%) and Cu (0.43% and 12.03%) content, suggesting these might represent surface compositions or concentrated areas of the deposited layers [51].Table 6 provides a general comparison between the four preparation methods, highlighting key results from the current study and relating them to findings from previous research. It demonstrates consistent outcomes across different studies for each preparation method [33,51].

Table 5. Quantitative analysis of the EDX spectra samples prepared by dip-coating and autoclave methods [33,51].

Substrates	**DD3-Clays**		**DD3-Clays +ZrO_2**	
Sample/Elements	**DD3**	**CZO-DD3**	**DD3 + ZrO_2**	**CZO-DD3 +ZrO_2**
O (at.%)	72.79	79.56	74.02	69.33
Al (at.%)	13.82	10.09	10.01	10.86
Si (at.%)	13.39	9.39	9.52	9.76
Zr (at.%)	-	-	6.45	7.96
Zn (at.%)	-	0.86	-	1.96
Cu (at.%)	-	0.11	-	0.13
O (at.%)	72.79	52.22	74.02	49.77
Zn (at.%)	-	47.34	-	38.20
Cu (at.%)	-	0.43	-	12.03

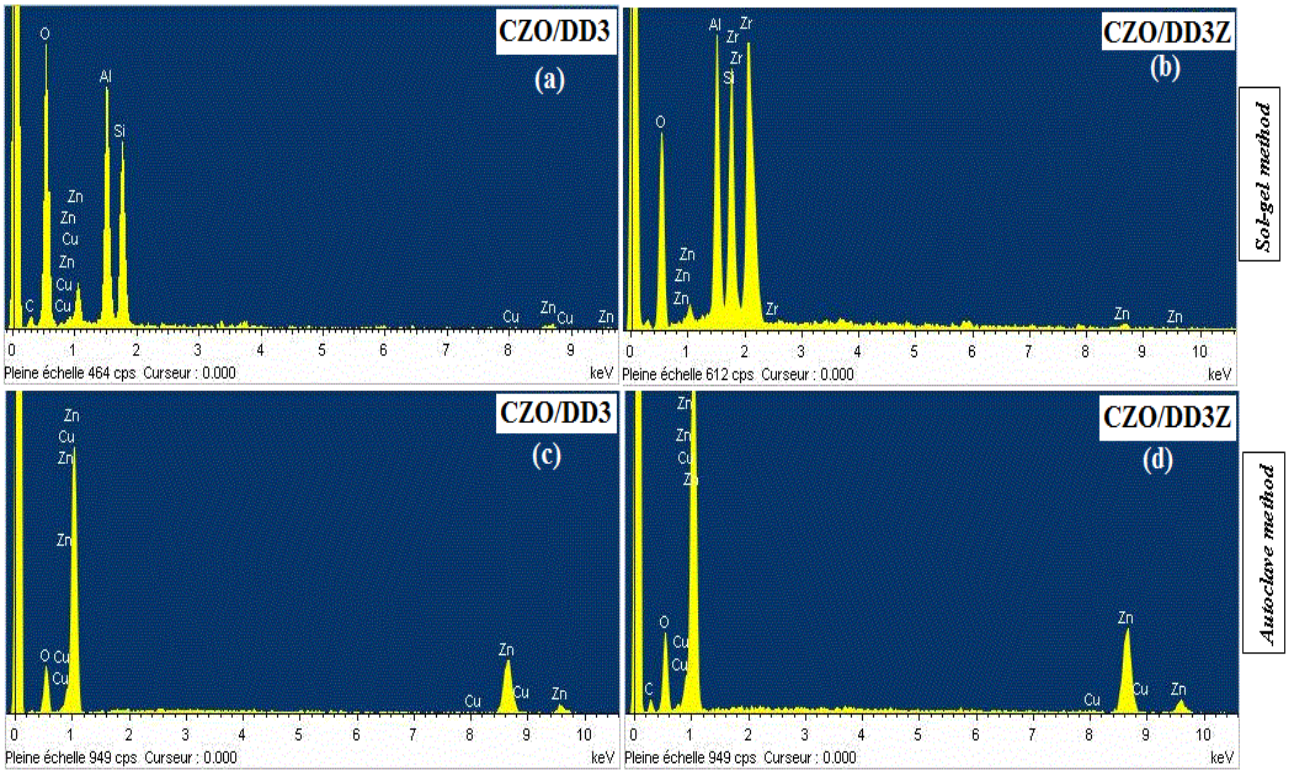


Figure 13. EDS spectrum of ceramic pellets after depositionofCu:ZnO thin layers with sol–gel and autoclave methods. Reprinted/adapted with permission of [33,51]. (**a**,**c**) Cu:ZnO/DD3, (**b**,**d**) Cu:ZnO/DD3 + 38 wt.% ZrO_2.

Table 6. Comparing the four preparation methods: mixing, co-precipitation, sol–gel, and autoclave.

Preparation Method	Current Results	Previous Results	Comparison	Ref.
Mixing	Heterogeneous structures	Tahir et al. (2024): Ultrasound-assisted MgO NPs for textile dye degradation	Both studies show enhanced dye degradation through particle size control	[86]
Co-precipitation	Finer particles, better dispersion	Gatou et al. (2024): MgO NPs for RhB/Rh6G degradation under sunlight	Confirms superior dispersion leads to improved visible-light activity	[87]
Sol–gel (dip-coating)	Uniform, fine-grained surfaces	Singaram & Selvaraj (2024): Green-synthesized MgO NPs for acid violet dye degradation	Validates that surface uniformity correlates with photocatalytic efficiency	[88]
Autoclave	Larger crystallites	Elashery et al. (2023): MgO–bentonite nanocomposites for crystal violet degradation	Both demonstrate hydrothermal methods favor crystalline growth for adsorption	[89]

3.3. Vibrational Spectroscopy

Infrared spectrophotometry is a valuable tool for studying materials' structures, compositions, and chemical properties [88]. Figure 14 presents the absorption bands observed across the range of 400–2000 cm^{-1} for ceramic powders (DD3 and DD3Z) with and without varying proportions of MgO, ZnO, and CuO [52–54], prepared using traditional mixing and co-precipitation methods and treated at 500 °C for two hours [52,53]. The powders' spectra indicate distinct features corresponding to mullite–cristobalite (DD3) and mullite–zircon

(DD3 + 38% ZrO_2) [52,53], consistent with the X-ray analysis results [52,53]. Absorption lines are attributed to bonds such as Al-O, Si-O, Zr-O, and Si-O-Al vibrations.

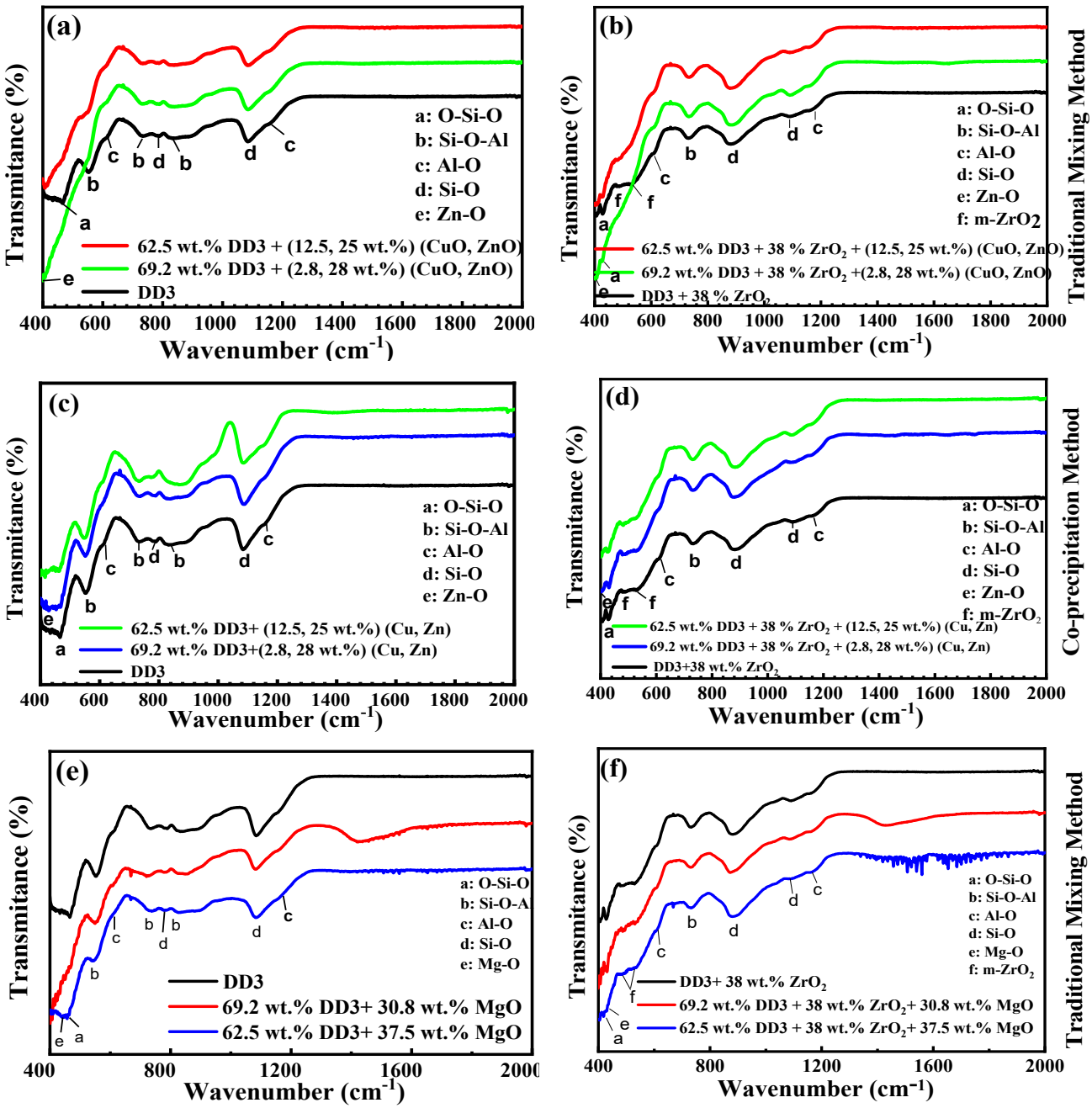


Figure 14. Infrared spectra of the ceramic powders with the addition of ZnO, CuO, and MgO. Reprinted/adapted with permission of [52,53]. (**a**,**b**) Co-precipitation method; (**c**–**f**) traditional mixing method.

Powders prepared via traditional mixing methods (Figure 14c,d) [52] exhibit changes in the absorption curve within the range of 400–590 cm^{-1}, notably reducing the pronounced peak around ~408 cm^{-1} associated with Zn–O and Cu–O vibrations [51]. Additionally, the introduction of MgO is marked by a distinct absorption band at ~420 cm^{-1} [53]. In contrast, powders prepared by the co-precipitation method (Figure 14e,f) [52] show consistent absorption curves even after the addition of compounds (ZnO, MgO, CuO), with a characteristic ZnO band observed at ~424 cm^{-1} [51]. This methodological difference

highlights the ability to differentiate between the ZnO spectrum and absorption bands using the mixing methods [89].

Overall, infrared spectroscopy provides insights into the chemical compositions and interactions affecting the stability of materials, showcasing differences between preparation methods through distinctive absorption features in the spectra [88,89]. Also, Figure 14 compares infrared spectra of ceramic powders prepared by co-precipitation (Figure 14a,b) [51] and traditional mixing (Figure 14c–f) methods [51,52] before and after adding ZnO, CuO, and MgO. In the mixing method, changes are observed in the 400–590 cm^{-1} range, with a reduction in the peak associated with Zn–O and Cu–O vibrations [51]. MgO addition creates a distinct band [52]. The co-precipitation method shows consistent absorption curves even after adding compounds with a characteristic ZnO band. This phenomenon suggests that the mixing method allows better ZnO spectrum and absorption band differentiation than co-precipitation [90].

During the examination of the chemical compositions of ceramic substrates, similar infrared spectra are observed both before and after the deposition of ZnO and Cu layers [51]. The distinguishing factor lies in the wavelength range of 400–1250 cm^{-1} (Figure 15a,b) [51]. In cases where the deposited layers exhibit high porosity, such as DD3 + ZrO_2, and with increased doping levels, peak intensity is noticeable. These peaks display significantly higher intensity compared to DD3 substrates [51]. This observation aligns with the results of EDX analysis, which indicate a higher percentage of dopants within the pores [91]. This combination of infrared spectroscopy and EDX analysis confirms that the presence of porosity and increased doping levels significantly influences the intensity and characteristics of infrared absorption peaks in these ceramic substrates [91].

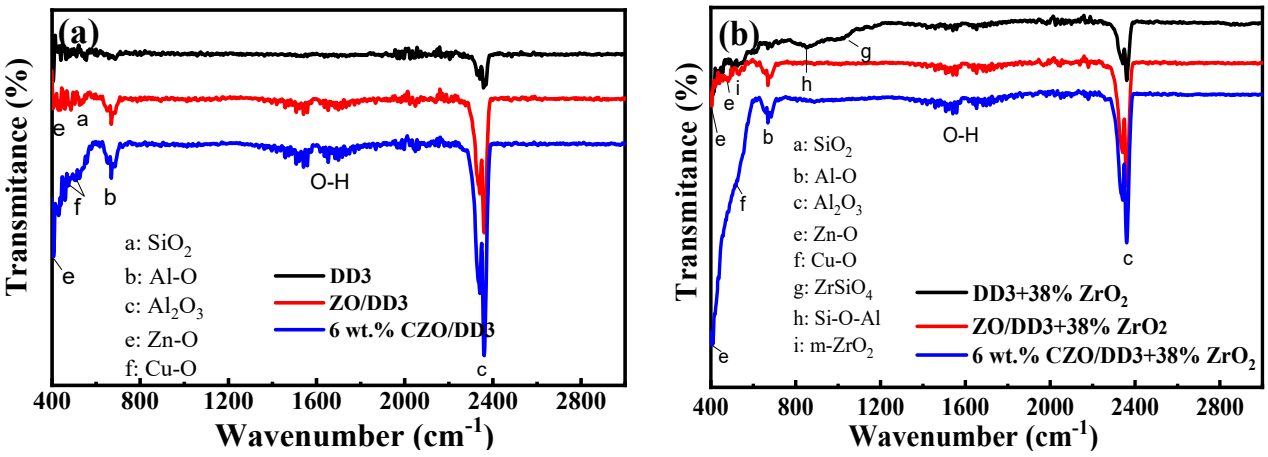


Figure 15. Infrared spectra of theceramic's pellets after deposition of Cu:ZnO thin layers with autoclave method. Reprinted/adapted with permission of [51]. (**a**) Cu:ZnO/DD3, (**b**) Cu:ZnO/DD3 + 38 wt.% ZrO_2.

The comparative analyses of FTIR spectra from Dikra Bouras et al. [53], Karina Bano et al. [92], and Luis M. Anaya-Esparza et al. [93] reveal distinct differences and similarities in the absorption bands observed across various materials. Dikra Bouras et al. [53] Table 7, identified significant absorption peaks at 553.23, 730.17, and 831.36 cm^{-1}, associated with Si–O–Al, with additional bands at 1170 cm^{-1} (Al–O bond) and 374 cm^{-1} (Si–O bond). The spectrum also showed a new absorption at 886 cm^{-1} after zirconium oxide addition and at 431 and 1443 cm^{-1} with 30 wt.% Mg, corresponding to Mg–O bonds. Karina Bano et al. [92] reported small distinct peaks between 400 and 750 cm^{-1}, indicative of Cu–O and Zn–O bonds in CuO/ZnO heterojunctions. Luis M. Anaya-Esparza et al. [93] observed bands at 667, 654, 604, and 543 cm^{-1} in TiO_2-ZnO-MgO nanomaterials, consistent with Ti–OH,

Ti–O, and Zn–O bonds, with additional peaks at 1600 cm^{-1} (O–H vibrations) and around 1500 cm^{-1} (O=C–O and C=O stretching). Each study emphasizes unique spectral features tied to the specific metal oxides and composites analyzed.

Table 7. Previous studies on infrared spectroscopy of various metal oxide compounds and composites reveal characteristic absorption bands for different chemical bonds [51–53,92,93].

Compound	Preparation Method	Key IR Bands (cm^{-1})	Ref.
TiO_2-ZnO-MgO	Sol–gel	667, 654, 604, 543 (TiO_2); 545 (Zn–O); 667 (MgO)	Anaya-Esparza et al. [93]
CuO/ZnO	Hydrothermal	400–750 (Cu–O and Zn–O)	Bano et al. [92]
DD3 and DD3Z (mullite-based)	Traditional mixing	408 (Zn–O, Cu–O); 420 (MgO)	Bouras et al. [52,53]
DD3 and DD3Z (mullite-based)	Co-precipitation	424 (ZnO)	Bouras et al. [52]
DD3 and DD3Z (mullite-based)	Autoclave	400–1250 (distinguishing range)	Bouras et al. [51]

4. Photocatalysis of Dyes

The photocatalytic degradation of organic dyes begins with light absorption by a semiconductor photocatalyst [94]. When the energy of the absorbed photons equals or exceeds the bandgap energy of the semiconductor, electron–hole pairs are generated within the material. This initial step is crucial for initiating the photocatalytic process [94]. Once formed, these electron–hole pairs can follow two primary pathways. They may recombine, releasing energy as heat, which is an undesirable outcome as it reduces the efficiency of the photocatalytic process. Alternatively, and more importantly for dye degradation, these charge carriers can migrate to the surface of the semiconductor, where they interact with adsorbed species [95].

At the semiconductor surface, electrons typically transfer to electron acceptors like oxygen molecules, forming superoxide radicals ($\bullet O_2^-$). Simultaneously, holes can interact with electron donors such as water or hydroxide ions, producing highly reactive hydroxyl radicals ($\bullet$OH) [96]. These radicals, particularly hydroxyl radicals, are powerful oxidizing agents capable of breaking down complex organic molecules like dyes [95,96]. The organic dye molecules, often adsorbed onto the photocatalyst surface, are then attacked by these reactive species. This leads to a series of oxidation reactions that progressively break down the dye's molecular structure [97]. The process typically involves the cleavage of chromophore groups responsible for the dye's color, followed by further decomposition of the resulting fragments [97].

Ideally, the end products of this degradation process are simple, harmless substances like carbon dioxide and water, representing the complete mineralization of the dye [96,97]. However, the efficiency and completeness of this process can vary depending on factors such as the nature of the photocatalyst, the specific dye being degraded, and the reaction conditions [98]. Photocatalysis represents a promising application of ceramics due to their nature abundance, cost-effectiveness, and environmental friendliness [99]. This technology is particularly significant because it can degrade, reduce, and mineralize hazardous organic compounds into harmless CO_2 and H_2O [100]. It finds extensive use in reducing toxic metal ions, disrupting waterborne microorganisms, and decomposing air pollutants into volatile organic compounds [101].

Photocatalysis operates based on advanced oxidation or reduction processes initiated by the excitation of electrons following photon absorption [102]. In this mechanism, semiconductors serve as active catalysts by facilitating the generation of electron–hole pairs under light irradiation [103]. While ZnO and CuO have been widely studied, several other metal oxides have also demonstrated strong photocatalytic activity under different lighting conditions. TiO_2, one of the earliest and most extensively explored photocatalysts, functions mainly under UV light by promoting electron excitation from the valence band to the conduction band, leading to the production of superoxide ($\bullet O_2^-$) and hydroxyl radicals (•OH) capable of oxidizing organic molecules [103]. MgO, though traditionally considered less active under visible light, can enhance photocatalytic efficiency through the introduction of surface defects, which act as active sites for radical generation and improve charge carrier separation [87]. Fe_2O_3 (hematite), with a narrower bandgap (~2.1 eV), is particularly attractive for visible-light-driven photocatalysis; it facilitates surface oxidation processes but often requires strategies to mitigate fast electron–hole recombination [81]. WO_3 (tungsten trioxide) offers strong absorption in the visible range and promotes photocatalytic reactions primarily through the activity of valence band holes that generate hydroxyl radicals, contributing significantly to pollutant degradation [85]. Together, these examples underline the critical roles played by material properties such as bandgap energy, crystallinity, surface morphology, and defect structures in determining photocatalytic performance. A comprehensive understanding of these factors is essential for the rational design of efficient photocatalysts for environmental applications. Overall, the photocatalytic mechanism closely resembles heterogeneous catalysis, where oxidation and reduction reactions are triggered at the semiconductor surface [52,103].

Photodynamics in photocatalysis hinges on the creation of electron–hole pairs within semiconductors upon absorbing photons with energy equal to or exceeding the bandgap energy ($h\nu \leq Eg$) (Equation (1)) [104]. Subsequent to photon absorption and the formation of electron–hole pairs (e−/h+) within the solid mass, these pairs undergo either recombination through heat release or interaction with species absorbed on the semiconductor surface [104]. Electrons migrate to acceptor molecules (A) in the fluid phase (gas or liquid) based on their redox potential (Equation (2)), while holes transfer to donor molecules (D) (Equation (3)) [105].

This process generates highly effective free radicals, facilitating oxygen regeneration and water oxidation (Equations (4) and (5)) [52,53,105]. The production of hydroxyl radicals (•OH) is particularly efficient during photocatalysis, effectively reducing the concentration of various chemical compounds and decomposing them with a high oxidation capacity (2.8 eV), surpassing that of other oxidants such as O_2 (2.42 eV) and H_2O_2 (1.78 eV) [106]. Additional oxidants like HO and H_2O_2 may also arise, potentially leading to intermediate product formation and the mineralization of chemical compounds absorbed on the photocatalyst surface [107]. The following chemical equations can summarize these mechanisms.

$$h\nu + (SC) \rightarrow h^+ + e^- \quad (1)$$

$$A(ads) + e^- \rightarrow A^-(ads) \quad (2)$$

$$D(ads) + h^+ \rightarrow D^+(ads) \quad (3)$$

$$H_2O + h^+ \rightarrow \bullet OH + H^+ \quad (4)$$

$$O_2 + e^- \rightarrow \bullet O_2^- + 4H^+ \quad (5)$$

The comparison in Table 8 highlights the evolution of photocatalytic research, showing a trend towards more diverse and efficient photocatalysts, a deeper understanding of reaction mechanisms, and a more holistic approach to assessing the environmental impact and practical applicability of photocatalytic dye degradation processes [108].

Table 8. Providing context on how current understanding compares with earlier research [109–115].

Aspect	Earlier Studies	Current Understanding	Ref.
Photocatalyst materials	Focused primarily on TiO_2	Expanded to include various metal oxides, composites, and doped materials	[109]
Light source	Mainly UV light	Increased emphasis on visible light activation through doping and sensitization	[110]
Reaction mechanism	Basic understanding of radical formation	More detailed elucidation of intermediate steps and species involved	[111]
Efficiency metrics	Often limited to color removal	Now includes total organic carbon (TOC) reduction and identification of intermediates.	[112]
Environmental factors	Limited consideration	Greater emphasis on pH, temperature, and water matrix effects	[113]
Scale of study	Mostly laboratory scale	Increasing number of pilot and industrial-scale studies	[114]
Byproduct analysis	Limited	More comprehensive analysis of transformation products and toxicity assessment	[115]

4.1. Photocatalytic Performance

4.1.1. The Catalytic Performance of Powders

Figure 16 illustrates the effectiveness of powders prepared via the mixing method using two ceramic types (DD3 and DD3 + 38% ZrO_2), both with and without additions of ZnO, CuO, and MgO, in purifying and analyzing OII-polluted solutions through absorbance spectra under ultraviolet light [52,53]. Initially, the powders without metal-oxide additions achieved a degradation efficiency of 42% for DD3 (Figure 16a) and 60.3% for DD3 + 38% ZrO_2 (Figure 16b) [52] over 7 h and 2 h, respectively [53]. After incorporating zinc oxide (ZnO) and copper oxide (CuO) via the traditional mixing method to enhance organic dye degradation [52], DD3-based powders achieved a degradation rate of 93.6% within 30 min, whereas DD3 + 38% ZrO_2 reached the same percentage in just 15 min under visible light exposure [52]. Additionally, the addition of MgO to ceramic powders demonstrated high efficiency in degrading OII-contaminated solutions, with degradation rates of 77.3% for DD3Z and 74.13% for DD3 after only 5 min [53].

The pH evolution during photocatalytic degradation was monitored using a calibrated pH meter. The initial Orange II solution in distilled water showed a pH of 6.8 ± 0.2. Under illumination, the pH decreased to 5.2 ± 0.3 after 60 min due to the formation of acidic intermediates (e.g., carboxylic acids) and proton release from the catalyst surface. In dark adsorption tests, the pH remained stable (6.5–6.7), confirming illumination-dependent acidification. This pH shift may influence the catalyst surface charge (PZC ~7.5 for ZnO) and dye molecule ionization. Post-reaction XRD confirmed catalyst stability, showing no phase changes and minimal metal leaching (<0.5 ppm Zn/Cu) after five cycles.

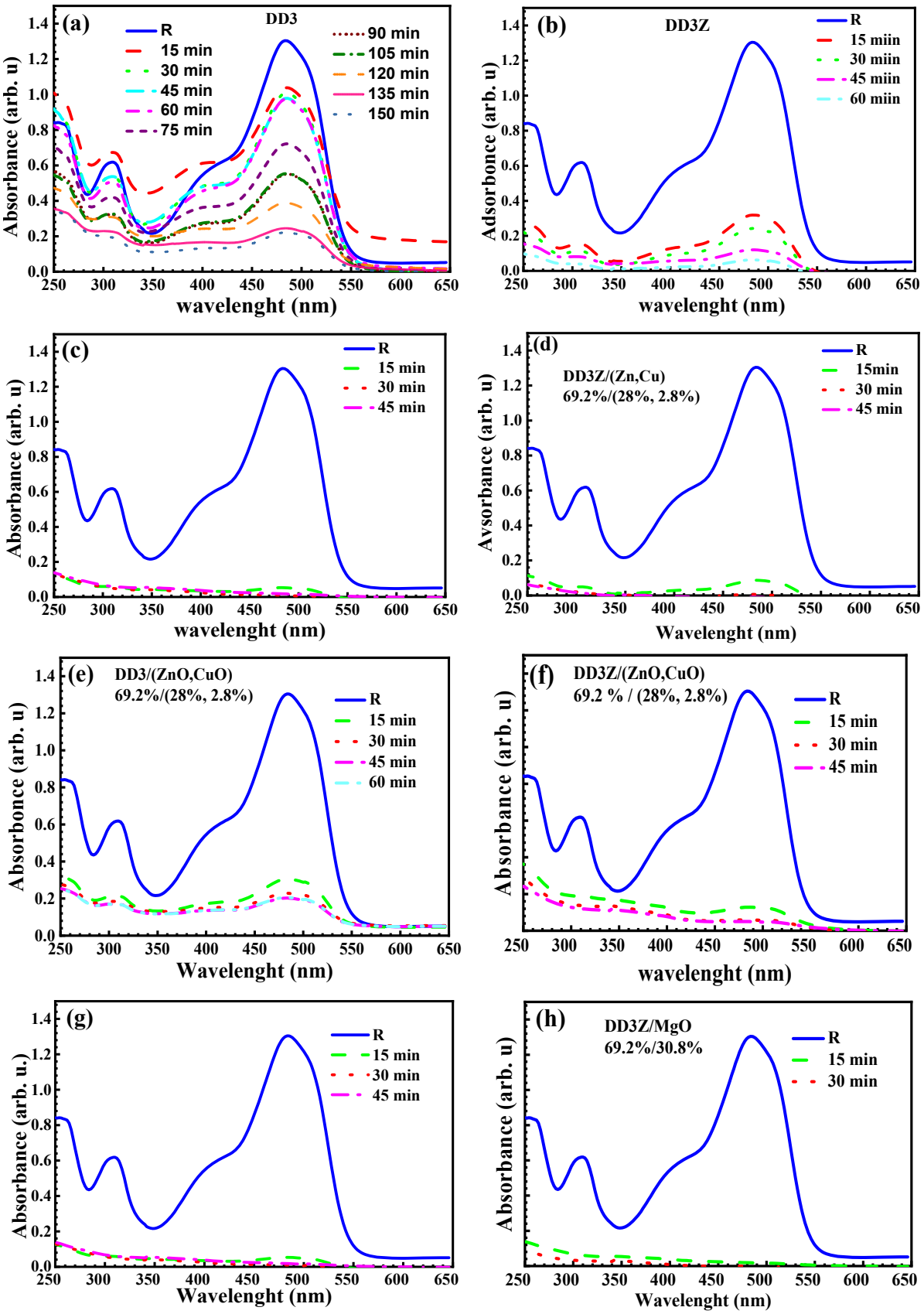


Figure 16. UV spectra of ceramic powders prepared with co-precipitation and mixed powder methods for degradation of OII (λ_{max} = 484 nm). Reprinted/adapted with permission of [52,53]. (**a**) DD3, (**b**) DD3 + 38 wt.% ZrO_2, (**c**,**e**) DD3/28 wt.% ZnO/2.8 wt.%CuO, (**d**,**f**), DD3Z/28 wt.% Zn/2.8 wt.% CuO, (**g**) DD3/30.8 wt.% MgO and DD3Z/30.8 wt.% MgO (**h**).

Powders prepared using the co-precipitation method, following the addition of 28 wt.% ZnO/2.8 wt.% CuO [52] to both ceramic types, exhibited notable degradation results in UV–visible spectra. Specifically, DD3-based powders achieved a degradation rate of 84.1% after 150 min, while DD3 + 38% ZrO_2 powders reached 99.6% degradation within 45 min [52]. Figure 17 illustrates the photocatalytic degradation of Orange II dye using different additives (ZnO, CuO, and MgO) treated at 500 °C [52,53]. The graph shows the degradation efficiency over time for various compositions. The pure DD3 and DD3Z samples exhibit relatively low photocatalytic activity. However, the addition of metal oxides significantly enhances the degradation rate. Notably, the samples containing ZnO show the highest degradation efficiency, with DD3Z + 10 wt.% ZnO performing best, achieving nearly complete degradation within 120 min [52]. The CuO-containing samples also show improved performance compared to the base materials, while MgO additions appear to have a lesser impact on the photocatalytic activity [53]. This comparative study demonstrates the effectiveness of ZnO as a photocatalytic enhancer for these ceramic composites in the degradation of Orange II dye [116]. Also Table 9 Photocatalysis in previous studies using samples prepared with various methods [117–122].

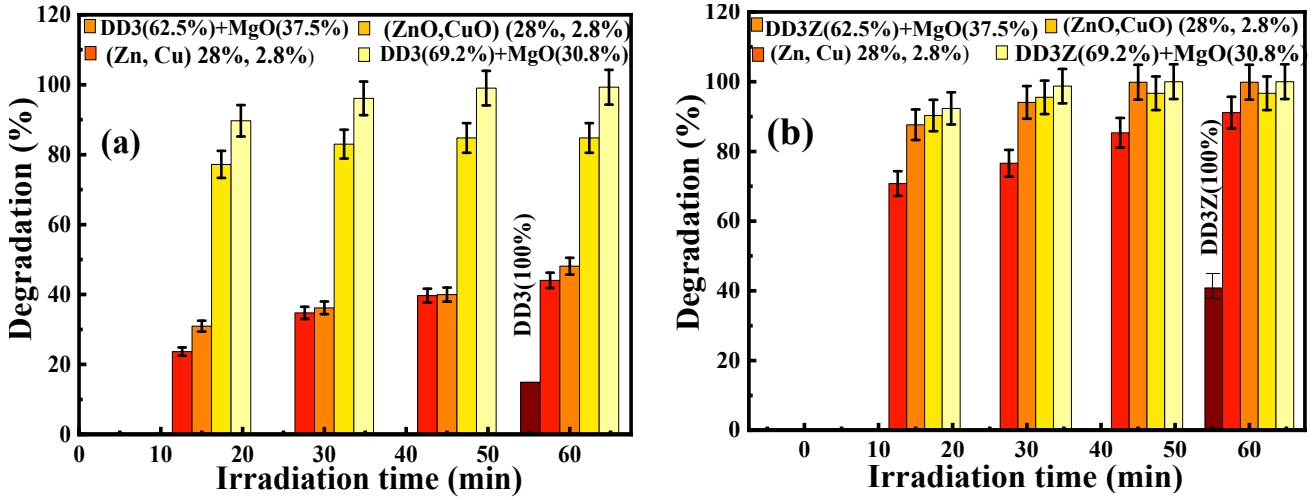


Figure 17. Degradation of Orange II of (**a**) DD3 and (**b**) for DD3Z with different additions of ZnO, CuO, and MgO, with a treatment at 500 °C (λ_{max} = 484 nm). Reprinted/adapted with permission of [52,53].

Table 9. Photocatalysis in previous studies using samples prepared with various methods [117–122].

Photocatalyst	Preparation Method	Pollutant	Light Source	Degradation Efficiency	Time	Ref.
ZnO/TiO_2	Sol–gel	MB	Visible light	92.3%	120 min	[117]
CdO/ZnO	Co-precipitation	Methylene Blue	UV light	94.8%	90 min	[118]
Graphene-ZnO	Hydrothermal	Rhodamine B	Visible light	96.2%	60 min	[119]
rGO-ZnO	Solution combustion	Para-nitro phenol	Visible light	97.1%	75 min	[120]
CuO/ZnO	Insitu deposition	Tetracycline	Sunlight	94%	50 min	[121]
$SnO_2/ZnO/TiO_2$	Sol–gel spin	Organic dyes	UV-Vis	98.5%	180 min	[122]

4.1.2. The Catalytic Performance of DD3-Based Layer Samples

The impact of ceramic substrates (DD3, DD3 + ZrO_2) with and without active Cu-doped ZnO thin films, fabricated using both autoclave and sol–gel methods [33,51], was investigated for their practical applicability in liquid purification [33,51]. Distilled water intentionally contaminated with OII was used as the test solution. The study utilized infrared spectroscopy, as depicted in Figure 17 [33,51], to analyze the evolution of absorbance spectra following exposure to ultraviolet (UV) radiation. For DD3-based substrates, the absorption spectra showed minimal change, with a reduction rate not exceeding 10% regardless of UV exposure time, even with active layers [33]. Similar behavior was observed for DD3 + ZrO_2 porous substrates before the deposition of thin layers [33]. However, upon deposition of ZnO thin films, the degradation rate increased to 77.7% for the same substrate type after 6 h of UV exposure [33].

Using the autoclave method to deposit the ZnO layer on DD3 + ZrO_2 substrates (Figure 18) [51], the absorbance spectra demonstrated significant efficacy, achieving an 81.1% degradation rate over 6 h. Conversely, the photocatalytic activity of layers deposited on DD3 substrates with the same doping and exposure time yielded a lower degradation rate of 36.1%. This discrepancy is attributed to the enhanced open porosity of the DD3 + ZrO_2 substrate, which facilitates the deposition of ZnO and CuO particles during sedimentation [51].

Overall, both types of ceramics exhibited enhanced photocatalytic performance when the autoclave method was employed compared to the sol–gel method, highlighting the role of substrate porosity and effective deposition of active layers in enhancing photocatalytic efficiency [123]. Figure 19 compares the degradation of Orange II dye using different preparation methods for the photocatalysts. The graph shows degradation efficiency over time for samples prepared via traditional mixing, co-precipitation, and autoclave methods [33,51–53]. The autoclave method consistently demonstrates superior performance across all compositions, achieving the highest degradation rates. The co-precipitation method generally shows intermediate performance [52], while the traditional mixing method exhibits the lowest degradation efficiencies [52,53]. Notably, the DD3Z + 10% ZnO sample prepared by the autoclave method achieves nearly complete degradation within 60 min, significantly outperforming the same composition prepared by other methods [52]. This comparison highlights the crucial role of the preparation method in determining the photocatalytic activity of these ceramic composites, with the autoclave method proving the most effective in enhancing the degradation of Orange II dye [124].

The photocatalytic activities of various photocatalysts were compared based on their effectiveness in degrading methylene blue (MB) and other pollutants under different light sources. Shokraiyan et al. [125] reported that ZnO/CuO nanocomposites exhibited high photocatalytic performance with 98% degradation of MB and 97% of 4-nitrophenol under LED light irradiation, as measured by decreases in their characteristic absorption peaks at 664 nm and 400 nm, respectively.

Büşra Çinar et al. [126] studied CuO–TiO_2 p-n heterostructures, finding that the optimal photocatalytic efficiency under UV light was achieved with 1.25 wt.% CuO, leading to a 99% degradation of MB in 45 min. In contrast, visible light irradiation showed lower activity with a maximum of 98% degradation at 0.5 wt.% CuO but only 59% at 1.0 wt.%. Meanwhile, Karina Bano et al. [92] highlighted that the CuO/ZnO heterojunctions were highly effective in removing tetracycline and ciprofloxacin, achieving 94% and 93% removal, respectively, within 50 min, demonstrating superior photocatalytic activity compared to pure CuO and ZnO [92]. These results underline the variability in photocatalytic efficiency depending on the material composition and the type of light used.

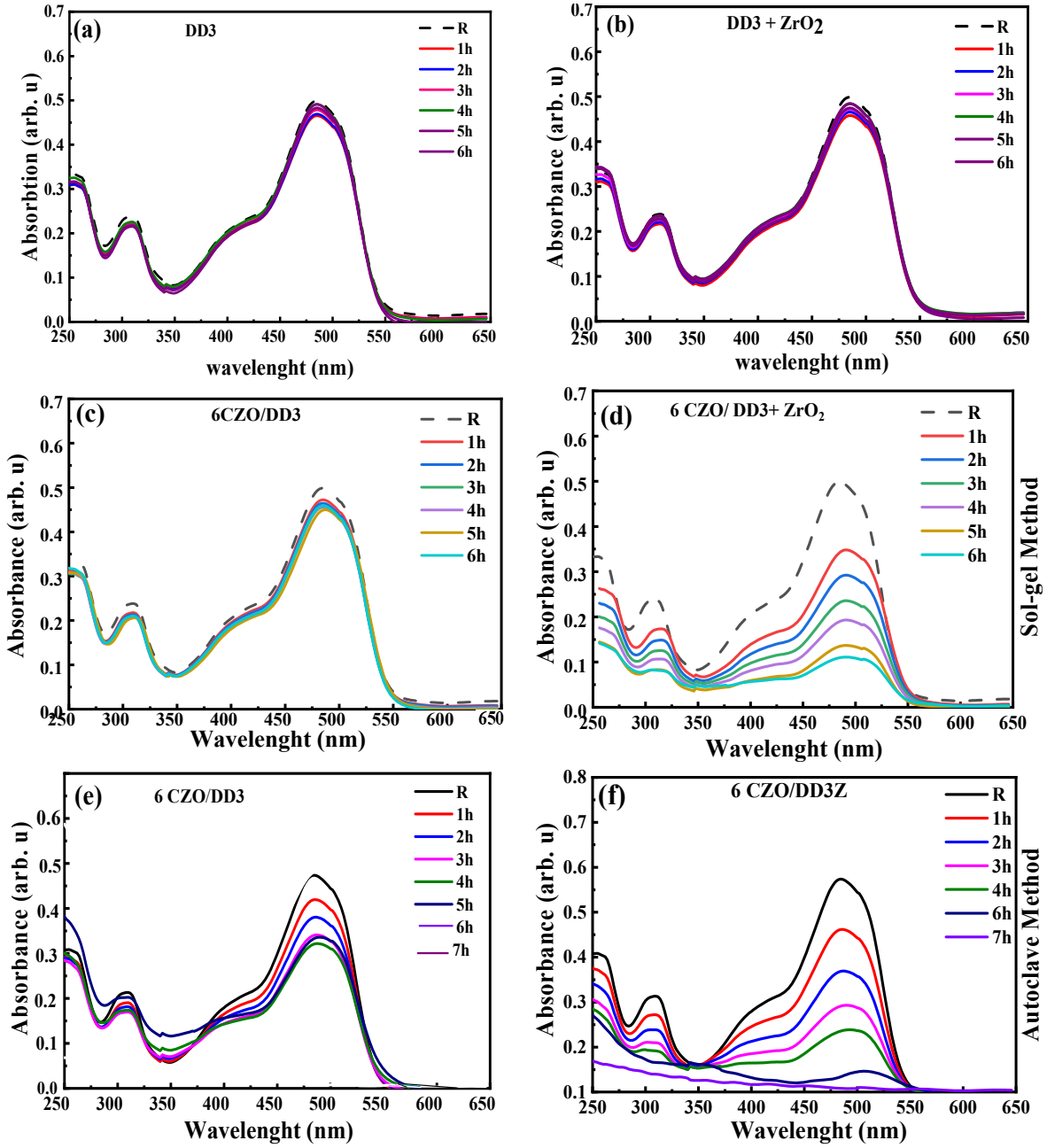


Figure 18. The degradation of OII by the (**a**–**d**) sol–gel method and (**e**,**f**) autoclave method for the pellets of DD3-clay and DD3 + ZrO_2-clay. Reprinted/adapted with permission of [33,51].

Tables 10 and 11 compares photocatalytic degradation of DD3 using powder and thin-film samples prepared by different methods. Powder samples generally show higher degradation rates than thin films. Adding 38% ZrO_2 to DD3 improves performance across methods. For powders, mixing with metal oxides (ZnO-CuO or MgO) significantly enhances degradation, with ZnO-CuO mixtures showing the highest rates (89.52% in 30 min, reaching 100% in 45 min). The co-precipitation method with ZrO_2 addition yields the best results for powders (99.6% in 45 min), achieving nearly complete degradation quickly. In thin films, sol–gel preparation with ZrO_2 and ZnO:Cu layers performs best, though less effectively than powders. Overall, combining DD3 with ZrO_2 and metal oxides like ZnO and CuO substantially improves photocatalytic activity, with preparation method greatly influencing performance.

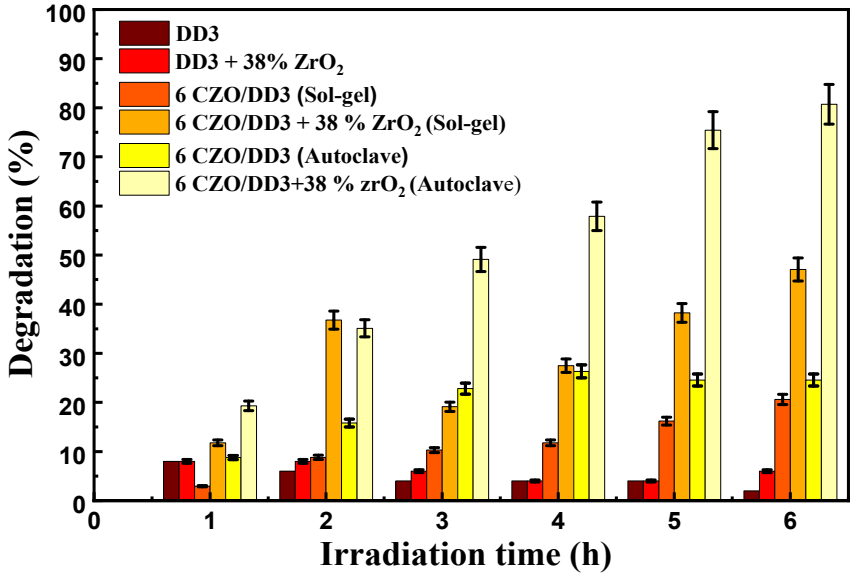


Figure 19. Degradation of Orange II with different methods: sol–gel and autoclave. Reprinted/adapted with permission of [33,51].

Table 10. Comparative results with the different methods [33,51–53].

Sample Type	Preparation Method	Material	Degradation (%)	Time
Powders	Mixing	DD3	42%	7 h
	Mixing	DD3 + 38% ZrO_2	63%	2 h
	Mixing	DD3/ZnO-CuO	89.52% (100% at 45 min)	30 min
	Mixing	DD3 + 38% ZrO_2/ZnO-CuO	96.35% (100% at 30 min)	15 min
	Mixing	DD3/MgO	74.1% (100% at 15 min)	5 min
	Mixing	DD3 + 38% ZrO_2/MgO	77.3% (100% at 10 min)	5 min
	Co-precipitation	DD3/ZnO-CuO	84.1%	150 min
	Co-precipitation	DD3 + 38% ZrO_2/ZnO-CuO	99.6%	45 min
Thin films	Sol–gel	DD3 substrate/ZnO:Cu layer	22%	6 h
	Sol–gel	DD3 + ZrO_2 substrate/ZnO:Cu layer	47%	6 h
	Autoclave	DD3 substrate/ZnO:Cu layer	25%	6 h
	Autoclave	DD3 + ZrO_2 substrate/ZnO:Cu layer	81.1%	6 h

Table 11. Previous studies on photocatalysis using metal oxide heterojunctions and nanocomposites show promising results for degrading various organic pollutants [92,125,126].

Photocatalyst	Preparation Method	Pollutant	Light Source	Degradation Efficiency	Time	Ref.
ZnO/CuO	Hydrothermal	MB	LED	98%	Not specified	[125]
ZnO-CuO	Hydrothermal	4-nitrophenol	LED	97%	Not specified	[125]
CuO-TiO_2 (1.25 wt.% CuO)	Hydrothermal	MB	UV	99%	45 min	[126]
CuO-TiO_2 (0.5 wt.% CuO)	Hydrothermal	MB	Visible	98%	4 h	[126]
CuO/ZnO	Hydrothermal	Tetracycline	Sunlight	94%	50 min	[92]
CuO/ZnO	Hydrothermal	Ciprofloxacin	Sunlight	93%	50 min	[92]

4.2. Mechanism of DD3Z/ZnO/CuO and DD3Z/MgO

The increased reliance on fossil fuels like petroleum and coal has led to fuel shortages and significant environmental issues, including global warming and air pollution. Additionally, the global production of organic pollutants such as synthetic dyes, pesticides, and fertilizers continues to harm the environment and living organisms [120]. In response, eco-friendly energy alternatives, including solar cells, hydropower, and clean hydrogen energy, are being explored to reduce environmental impact [127]. Among these, clean hydrogen energy stands out for its efficiency in producing clean energy and environmental protection. Various techniques, such as electrolytic processes, photochemical methods, and solar water splitting, are being developed for hydrogen production [128]. Photocatalysis, in particular, has emerged as a promising, cost-effective method for environmental applications, including water purification and pollutant degradation [129].

The determination of semiconductor positions is crucial and is referenced against the standard hydrogen electrode (SHE), coded as NHE (Figure 20) [33,35,51–53]. The conduction and valence band positions for ZrO_2, ZnO, CuO, and MgO at the zero-charge point were calculated using the following relationships [52,53].

$$E_{VB} = X - Ee + 0.5Eg \quad (6)$$

$$E_{CB} = E_{VB} - Eg \quad (7)$$

where E_{VB} represents the edge potential of the valence band, E_{CB} is the conduction band edge potential, X is the electronegativity value for semiconductors (X_{CuO} = 5.81 eV, X_{ZnO} = 5.79 eV, X_{ZrO2} = 5.92 eV, X_{MgO} = 5.2 eV, X_{NiO} = 5.75 eV, X_{Ag2O} = 5.2 eV, X_{MnO_2} = 5.315 eV) [33,51–53], Ee is the energy of the free electrons on the hydrogen scale ~4.5 eV, and Eg is the semiconductor gap energy. After applying the two relations on each element, the conduction and valence band value was found; the results are shown in Table 12 [52,53,130,131].

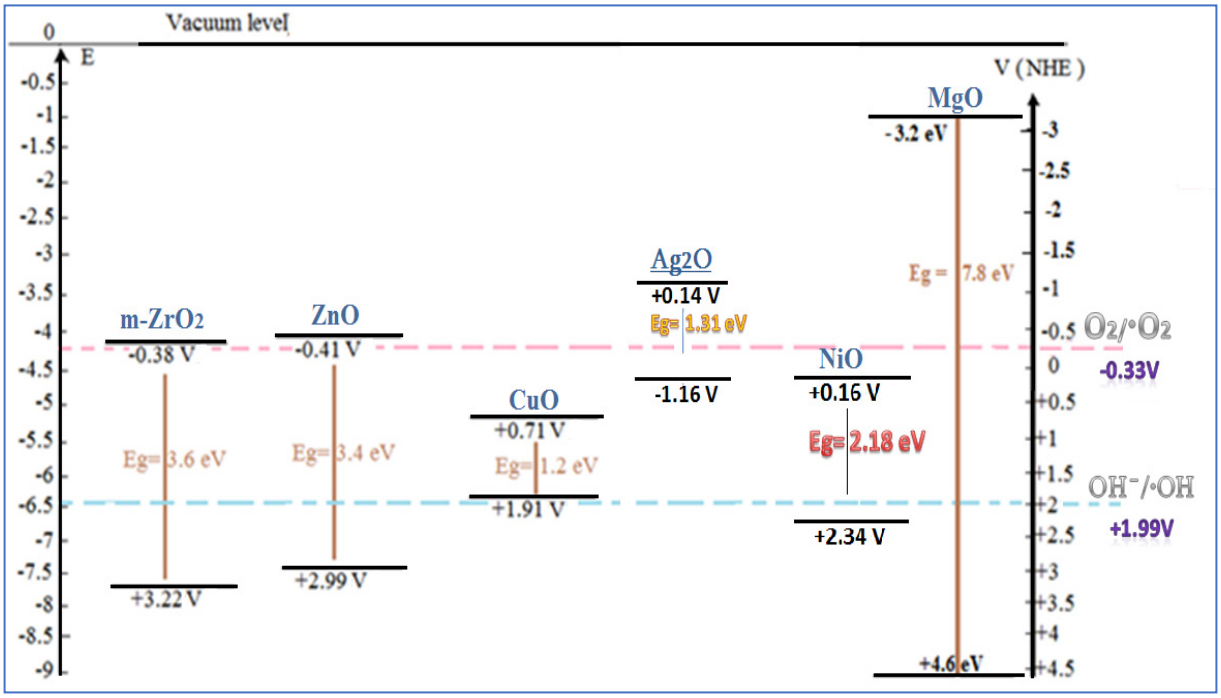


Figure 20. Band gap energy position for semiconductors according to the NHE scale.

Table 12. Values of the valence and conduction bands for each metal-oxide material.

Semiconductor	X	Ee	Eg	E_{CB}	E_{VB}
m-ZrO_2	5.92	4.5	3.6	−0.38	+3.22
ZnO	5.79	4.5	3.4	−0.41	+2.99
CuO	5.81	4.5	1.2	+0.71	+1.91
MgO	5.2	4.5	7.8	−3.2	+4.6
NiO	5.75	4.5	2.18	+0.16	+2.34
MnO_2	5.315	4.5	1.41	−0.01	+1.52
Ag_2O	5.2	4.5	1.31	−1.16	0.14

According to S. Nayak et al. [130], the oxidation potentials of the holes in the valence band need to be sufficiently positive to generate hydroxyl radicals. It is noted that the standard oxidation potential (E^{Θ} (OH^-/•OH)) required for the conversion of OH^- to •OH is +1.99 eV [44]. Conversely, the electrons in the conduction band must be negative enough to generate superoxide radicals [131], with the standard oxidation potential (EΘ (O_2/•O_2^-)) needed for the conversion of O_2 to •O_2^- being −0.33 eV [130]. When selecting oxides from various semiconductors, it is important to consider those with valence and conduction band levels most suitable for the mineralization of organic pollutants. Figure 21 summarizes these findings.

$$ZrO_2 + ZnO + CuO + MgO + h\upsilon \rightarrow ZrO_2\,(e^-) + ZnO\,(e^-) + CuO\,(e^-) + MgO\,(e^-) + ZrO_2\,(h^+) + ZnO\,(h^+) + CuO\,(h^+) + MgO\,(h^+) \quad (8)$$

$$ZnO\,(e^-) + MgO\,(e^-) + ZrO_2 \rightarrow ZrO_2\,(e^-) \quad (9)$$

$$CuO\,(e^-) + ZnO \rightarrow ZnO\,(e^-) \quad (10)$$

$$ZnO\,(h^+) + CuO \rightarrow CuO\,(h^+) \quad (11)$$

$$ZrO_2\,(e^-) + ZnO\,(e^-) + MgO\,(e^-) + O_2 \rightarrow \bullet O_2^- \quad (12)$$

$$ZrO_2\,(h^+) + ZnO\,(h^+) + MgO\,(h^+) + OH^- \rightarrow OH\bullet \quad (13)$$

$$ZrO_2\,(h^+) + ZnO\,(h^+) + MgO\,(h^+) + H_2O \rightarrow OH\bullet + H^+ \quad (14)$$

$$\bullet O_2^- + H_2O \rightarrow HO_2^- + OH^- \quad (15)$$

$$2HO_2^- \rightarrow H_2O_2 + O_2 \quad (16)$$

$$H_2O_2 + e^- \rightarrow OH\bullet + OH^- \quad (17)$$

$$OH\bullet + \text{Dey} \rightarrow \text{gradient dye} \quad (18)$$

$$OH\bullet + \bullet O_2^- + h_{VB}^+ + \text{gradient dye} \rightarrow CO_2 \uparrow + H_2O \quad (19)$$

The photocatalytic process relies on light-induced redox reactions to generate active radicals like hydroxyl (•OH) and superoxide (•O_2^-) for breaking down pollutants [131]. Effective photocatalysis depends on selecting materials that efficiently absorb sunlight and promote charge separation and transfer [132]. Metal-oxide nanomaterials like TiO_2, ZnO, WO_3, and Fe_2O_3 have been studied for their photocatalytic properties due to their diverse structures and optical characteristics [133]. Among these, TiO_2 and ZnO are particularly noted for their stability, photosensitivity, and non-toxic nature, making them effective for environmental cleanup [134].

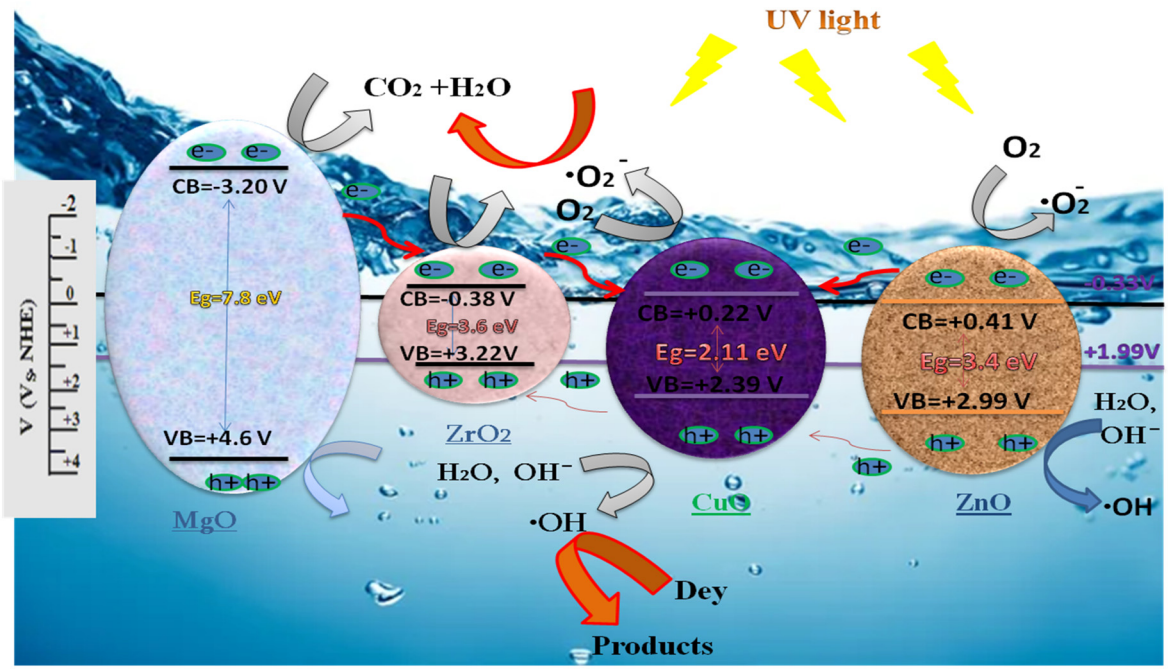


Figure 21. Mechanism of photocatalysis for the compound ZrO_2/CuO/ZnO/MgO.

ZnO is known for its suitable band gap (approximately 3.2–3.4 eV), allowing it to utilize visible light effectively [135]. However, issues such as rapid charge recombination and photo corrosion limit its efficiency. Strategies to enhance ZnO's photocatalytic performance include doping, forming nanocomposites or heterojunctions with other semiconductors, and modifying its nanostructure to improve light absorption and charge separation [135]. Despite its potential, the photocorrosion problem can be mitigated by coating ZnO with protective layers like graphene or carbon nanotubes, which enhance its stability and performance [136].

Overall, developing advanced photocatalytic materials and methods continues to be a key area of research to address environmental challenges and improve the efficiency of clean energy technologies [134–136].Based on the provided information, we can compare the photocatalytic performance of various ZnO- and CuO-based nanocomposites and heterojunctions [137]. The Ag/Ag_2O/ZnO ternary nanocomposite prepared by arching technique showed excellent performance in decomposing methylene blue (MB) under UV-light irradiation, outperforming single- and double-constituent catalysts [138]. The γ-Fe_2O_3-ZnO–biochar nanocomposite, synthesized via thermal decomposition, demonstrated the highest reported efficiency of 86.2% in degrading Rhodamine B (RhB) within 30 min [139]. Another notable performer (Table 13) was the Ag@ZnO/TiO_2 flexible hierarchical heterojunction, produced by hydrothermal and photodeposition processes, which achieved 91.6% degradation of tetracycline hydrochloride (TC-H) in 1 h [140]. The CuO-TiO_2 heterostructure also showed promising results in MB degradation under visible light, with hydroxyl radicals playing a key role in the photocatalytic process [140].

Overall, the photocatalytic composites demonstrated strong potential for dye degradation, although further investigations into mineralization pathways and by-product identification will be necessary to fully validate their environmental impact [120,121]. While the photocatalytic activity results, based on UV-Vis spectrophotometry, clearly demonstrated a rapid and significant decrease in the characteristic absorption peak of Orange II at 484 nm, it is essential to note that complete mineralization of the dye into CO_2 and H_2O cannot be conclusively confirmed using this technique alone [122]. The UV-Vis method primar-

ily monitors the disappearance of chromophoric groups but does not provide detailed information about intermediate products formed during degradation [123,124].

Table 13. Comparison of photocatalytic systems and their key features [52,53,138–141].

Photocatalyst	Preparation Method	Target Pollutant	Key Features	Band Gap (eV)	Conduction Band (eV)	Valence Band (eV)	Ref.
DD3Z/ZnO/CuO/MgO	Mixing/Co-precipitation	OII	Multi-component system, optimized band alignment	Varies	Varies	Varies	[52,53]
ZrO_2	-	OII	Component in new system	3.6	−0.38	+3.22	[52,53]
ZnO	-	OII	Component in new system, visible light active	3.4	−0.41	+2.99	[52]
CuO	-	OII	Component in new system	1.2	+0.71	+1.91	[52]
MgO	-	OII	Component in new system	7.8	−3.2	+4.6	[53]
Ag/Ag_2O/ZnO	Arching technique	Methylene blue	3D-flower-like architecture	Not specified	CB_{ZnO} = −0.34 eV CB_{Ag2O} = +0.19 eV	VB_{ZnO} = +2.86 eV VB_{Ag2O} = +1.39 eV	[138]
γ-Fe_2O_3-ZnO-biochar	Thermal de-composition	Rhodamine B	86.2% degradation in 30 min	Not specified	Not specified	Not specified	[139]
Ag@ZnO/TiO_2	Hydrothermal and photode-position	Tetracycline hydrochlo-ride	91.6% degradation in 1 h	Not specified	Not specified	Not specified	[140]
CuO-TiO_2	Hydrothermal	Methylene blue	Hydroxyl radicals as primary active species	Not specified	−0.25	+0.93	[141]

According to previous studies, Orange II degradation often proceeds through forming intermediate species such as aromatic amines, carboxylic acids, and nitrogen-containing compounds [125,126]. Without employing advanced analytical techniques like High-Performance Liquid Chromatography (HPLC), Gas Chromatography–Mass Spectrometry (GC-MS), Total Organic Carbon (TOC) analysis, or Ion Chromatography (IC), the identification and quantification of these intermediates remain unresolved [127–129].

Future work will incorporate such techniques to provide a more detailed understanding of the degradation pathway and the extent of mineralization achieved [130,131]. Combining photocatalysis with complementary advanced oxidation processes such as photo-ozonation is also a promising strategy [132,133]. Ozone could enhance hydroxyl radical production, accelerate oxidation kinetics, and promote deeper mineralization of persistent organic molecules, addressing the limitations of photocatalysis alone [134–136].

Some recent studies have successfully combined photocatalysis with ozonation, resulting in higher mineralization rates and shorter treatment times than photocatalysis alone, especially for complex dyes like Orange II [137–141].

5. Conclusions

This comprehensive review of photocatalytic material preparation methods yielded several key findings. Adding ZrO_2 to DD3 ceramics significantly altered grain structure and increased porosity, enhancing the material's potential for photocatalytic applications. They have been highlighted due to their natural abundance, affordability, ease of access, and favorable thermal and mechanical properties. Co-precipitation methods generally produce finer particles than traditional mixing, potentially leading to better dispersion and enhanced properties.

Sol–gel and autoclave methods for thin-film deposition resulted in distinct morphologies, with sol–gel producing more uniform flower-like shapes and finer-grained surfaces and autoclave methods yielding larger, more distinct crystallites. XRD analysis revealed the successful incorporation of metal oxides into the ceramic matrix, with observed peak shifts indicating structural distortions due to doping. The analysis confirmed a shift in spectra towards higher values, indicating smaller particle sizes with zinc and copper additions and larger particle sizes with magnesium oxide additions. SEM imaging demonstrated that the addition of ZnO, CuO, and MgO increased porosity and altered surface morphology, creating structures suitable for capturing pollutants. EDX analysis confirmed the successful incorporation of dopant elements, with varying concentrations depending on the preparation method and substrate used.

The photocatalytic testing setup for Orange II dye degradation was described, setting the stage for future performance evaluations. During powder preparation, after adding zinc and copper oxides, the decomposition rate reached 93.63% within a short period of 15 min. When magnesium oxide was added to the ceramic material, the photocatalytic efficiency surpassed that of the previous materials, achieving complete pigment dissolution in under 10 min. Upon depositing Cu thin layers on both types of ceramic samples, the absorption capacity of samples prepared via the autoclave method exceeded that of samples prepared via the sol–gel method.

These findings contribute to understanding how different preparation methods and dopants affect the properties of ceramic-based photocatalysts. This study provides a foundation for optimizing these materials for environmental applications, particularly in the degradation of organic pollutants in water. Future research should focus on quantifying the photocatalytic performance of these materials and exploring their potential for large-scale water treatment applications.

Funding: This work was supported and funded by the Deanship of Scientific Research at Imam Mohammad Ibn Saud Islamic University (IMSIU) (grant number IMSIU-DDRSP2502).

Data Availability Statement: No new data were created or analyzed in this study.

Conflicts of Interest: The authors declare no conflicts of interest.

References

1. Bouras, D.; Fellah, M.; Barillé, R.; Iqbal, A.; Fouzia, H.; Aleksei, O.; El-Hiti, G.A. Thin layers of Fe-doped ZnO deposited by spin-coating for electrolysis and photodetector applications. *Trans. Nonferrous Met. Soc. China* **2025**, *35*, 1262–1280. [CrossRef]
2. Al-Tohamy, R.; Ali, S.S.; Li, F.; Okasha, K.M.; Mahmoud, Y.A.-G.; Elsamahy, T.; Jiao, H.; Fu, Y.; Sun, J. A critical review on the treatment of dye-containing wastewater: Ecotoxicological and health concerns of textile dyes and possible remediation approaches for environmental safety. *Ecotoxicol. Environ. Saf.* **2022**, *231*, 113160. [CrossRef] [PubMed]
3. Bouras, D.; Fellah, M.; Barille, R.; Grigorian, S.; El-Hiti, G.A. Innovative ceramic solutions: Boosting antibacterial power of $DD3_{0.85}Mg_{0.15}O$ for environmental applications. *Inorg. Chem. Commun.* **2025**, *174*, 114046. [CrossRef]
4. Sharma, A.K.; Sharma, M.; Sharma, A.K.; Sharma, M. Mapping the impact of environmental pollutants on human health and environment: A systematic review and meta-analysis. *J. Geochem. Explor.* **2023**, *255*, 107325. [CrossRef]
5. Haque, N. Exploratory analysis of fines for water pollution in Bangladesh. *Water Resour. Ind.* **2017**, *18*, 1–8. [CrossRef]

6. Bouras, D.; Fellah, M.; Barille, R.; Zerouali, M.; Hambli, N.; El-Hiti, G.A. Comparative study of zirconium-zinc oxide thin films on ceramic and glass substrates: Structural, optical, and photocatalytic properties. *Inorg. Chem. Commun.* **2025**, *171*, 113561. [CrossRef]
7. Rajmohan, K.S.; Chandrasekaran, R.; Varjani, S. A Review on Occurrence of Pesticides in Environment and Current Technologies for Their Remediation and Management. *Indian J. Microbiol.* **2020**, *60*, 125–138. [CrossRef]
8. Boumous, Z.; Boumous, S.; Fellah, M.; Habeeb, M.A.; Latréche, S.; Grigorian, S.; El-Hiti, G.A. Synthesis, polarization currents, dielectric constant, and stability of magnesium titanate-based ceramics. *J. Mater. Sci. Mater. Electron.* **2025**, *36*, 611. [CrossRef]
9. Hashemi, S.H.; Kaykhaii, M. Chapter 15—Azo dyes: Sources, occurrence, toxicity, sampling, analysis, and their removal methods, Emerging Freshwater Pollutants Analysis, Fate and Regulations. In *Emerging Freshwater Pollutants*; Elsevier: Amsterdam, The Netherlands, 2022; pp. 267–287. [CrossRef]
10. Bouras, D.; Fellah, M.; Barille, R.; Obrosov, A.; Ikbal, A.; Avramov, P.V.; El-Hiti, G.A. Multiple layers, porous surface, and their role in increasing the efficiency of photocatalytic coating on (DD3, DD3+ZrO_2) ceramics and glass. *Ceram. Int.* **2024**, *50*, 43854–43873. [CrossRef]
11. Dikra, B.; Fellah, M.; Barille, R.; Weiß, S.; Samad, M.A.; Alburaikan, A.; Khalifa, H.A.E.-W.; Obrosov, A. Improvement of photocatalytic performance and sensitive ultraviolet photodetectors using AC-ZnO/ZC-Ag_2O/AZ-CuO multilayers nanocomposite prepared by spin coating method. *J. Sci. Adv. Mater. Devices* **2024**, *9*, 100642. [CrossRef]
12. Saravanan, A.; Kumar, P.S.; Jeevanantham, S.; Karishma, S.; Tajsabreen, B.; Yaashikaa, P.; Reshma, B. Effective water/wastewater treatment methodologies for toxic pollutants removal: Processes and applications towards sustainable development. *Chemosphere* **2021**, *280*, 130595. [CrossRef]
13. Sellam, M.; Azizi, S.; Bouras, D.; Fellah, M.; Obrosov, A.; El-Hiti, G.A. Degradation of rhodamine B dye under visible and solar light on zinc oxide and nickel-doped zinc oxide thin films. *Opt. Mater.* **2024**, *151*, 115316. [CrossRef]
14. Gul, A.; Hruza, J.; Yalcinkaya, F. Fouling and Chemical Cleaning of Microfiltration Membranes: A Mini-Review. *Polymers* **2021**, *13*, 846. [CrossRef] [PubMed]
15. Lu, J.; Zhang, P.; Li, J. Electrocoagulation technology for water purification: An update review on reactor design and some newly concerned pollutants removal. *J. Environ. Manag.* **2021**, *296*, 113259. [CrossRef]
16. Stambouli, I.; Zerouali, M.; Daïra, R.; Bouras, D.; El-Hiti, G.A.; Grigorian, S.; Fellah, M. Enhancement of tin-doping on the structural, electrical, and optical properties of copper oxide thin films for optoelectronic applications. *Ceram. Int.* **2025**, *51*, 17689–17703. [CrossRef]
17. Baía, A.; Lopes, A.; Nunes, M.J.; Ciríaco, L.; Pacheco, M.J.; Fernandes, A. Removal of Recalcitrant Compounds from Winery Wastewater by Electrochemical Oxidation. *Water* **2022**, *14*, 750. [CrossRef]
18. Chen, X.H.; Tee, K.; Elnahass, M.; Ahmed, R. Assessing the environmental impacts of renewable energy sources: A case study on air pollution and carbon emissions in China. *J. Environ. Manag.* **2023**, *345*, 118525. [CrossRef]
19. Xu, Y.; Wen, S.; Tao, C.Q. Impact of environmental tax on pollution control: A sustainable development perspective. *Econ. Anal. Policy* **2023**, *79*, 89–106. [CrossRef]
20. Miranda Zoppas, F.; Sacco, N.; Soffietti, J.; Devard, A.; Akhter, F.; Marchesini, F.A. Catalytic approaches for the removal of microplastics from water: Recent advances and future opportunities. *Chem. Eng. J. Adv.* **2023**, *16*, 100529. [CrossRef]
21. Rim, I.; Hezil, N.; Fellah, M.; Saoudi, A.; Aleksei, O.; El-Hiti, G.A. Enhancing Kaolin Performance through Organic Molecule Modification and Assessing Its Efficiency for Lead and Copper Adsorption. *Environ. Technol. Innov.* **2024**, *36*, 103904. [CrossRef]
22. Long, Z.; Li, Q.; Wei, T.; Zhang, G.; Ren, Z. Historical development and prospects of photocatalysts for pollutant removal in water. *J. Hazard. Mater.* **2020**, *395*, 122599. [CrossRef]
23. Younis, S.A.; Kwon, E.E.; Qasim, M.; Kim, K.-H.; Kim, T.; Kukkar, D.; Dou, X.; Ali, I. Metal-organic framework as a photocatalyst: Progress in modulation strategies and environmental/energy applications. *Prog. Energy Combust. Sci.* **2020**, *81*, 100870. [CrossRef]
24. Mishra, B.K.; Kumar, P.; Saraswat, C.; Chakraborty, S.; Gautam, A. Water Security in a Changing Environment: Concept, Challenges and Solutions. *Water* **2021**, *13*, 490. [CrossRef]
25. Migani, A.; Blancafort, L. Theoretical Studies of Photochemistry on TiO_2 Surfaces. *Encycl. Interfacial Chem. Surf. Sci. Electrochem.* **2018**, 637–653. [CrossRef]
26. Singh, G.; Sharma, M.; Vaish, R. Emerging trends in glass-ceramic photocatalysts. *Chem. Eng. J.* **2021**, *407*, 126971. [CrossRef]
27. Mao, J.; Hong, W.; Li, Q.; Gao, Y.; Jiang, Y.; Li, Y.; Li, B.; Gao, B.; Xu, X. The application strategies and progresses of silicon-based minerals in advanced oxidation processes for water decontamination. *Coord. Chem. Rev.* **2024**, *511*, 215871. [CrossRef]
28. Song, B.; Wang, Z.; Li, J.; Ma, Y. Preparation and electrocatalytic properties of kaolin/steel slag particle electrodes. *Catal. Commun.* **2021**, *148*, 106177. [CrossRef]
29. Zhang, B.; Hou, Y.; Yu, Z.; Liu, Y.; Huang, J.; Qian, L.; Xiong, J. Three-dimensional electro-Fenton degradation of Rhodamine B with efficient Fe-Cu/kaolin particle electrodes: Electrodes optimization, kinetics, influencing factors and mechanism. *Sep. Purif. Technol.* **2019**, *210*, 60–68. [CrossRef]

30. Yang, M.; Lei, N.; Liu, J.; Yang, L.; Li, B.; He, X. Removal of heavy metal ions from wastewater by combined modified kaolin. *Desalination Water Treat.* **2018**, *103*, 152–162. [CrossRef]
31. Funsueb, N.; Thipboonraj, A.; Wannawek, A.; Pranamornkith, P.; Panthuwat, W. Physical properties and microstructure of traditional kaolin-based ceramics with additive fly–ash (FA). *J. Phys. Conf. Ser.* **2023**, *2431*, 012049. [CrossRef]
32. da Silva, W.; Hamilton, J.; Sharma, P.; Dunlop, P.; Byrne, J.; dos Santos, J. Agro and industrial residues: Potential raw materials for photocatalyst development. *J. Photochem. Photobiol. A Chem.* **2021**, *411*, 113184. [CrossRef]
33. Bouras, D.; Mecif, A.; Mahdjoub, A.; Harabi, A.; Zaabat, M.; Barille, R. Photocatalytic degradation of orange II by active layers of cu-doped ZnO deposited on porous ceramic Substrates. *J. Ovonic Res.* **2017**, *13*, 271–281.
34. Okpara, E.C.; Olatunde, O.C.; Wojuola, O.B.; Onwudiwe, D.C. Applications of Transition Metal Oxides and Chalcogenides and their Composites in Water Treatment: A review. *Environ. Adv.* **2023**, *11*, 100341. [CrossRef]
35. Bouras, D.; Fellah, M.; Barille, R.; Abdul Samad, M.; Rasheed, M.; Awjan Alreshidi, M. Properties of MZO/ceramic and MZO/glass thin layers based on the substrate's quality. *Opt. Quantum Electron.* **2024**, *56*, 104. [CrossRef]
36. Bouras, D.; Fellah, M.; Barillé, R.; Obrosov, A.; El-Hiti, G.A. Production of novel Zr–Mg nanoceramics based on kaolinite clay with strong antibacterial activity. *Ceram. Int.* **2024**, *16*, 27949–27960. [CrossRef]
37. Bouras, D.; Fellah, M.; Habeeb, M.A.; Aouar, L.; Barille, R.; El-Hiti, G.A. Structural and antibacterial activity of developed nano-bioceramic DD3/ZrO_2/ZnO/CuO powders. *J. Korean Ceram. Soc.* **2024**, *61*, 837–853. [CrossRef]
38. Sun, Y.; Zhang, W.; Li, Q.; Liu, H.; Wang, X. Preparations and applications of zinc oxide based photocatalytic materials. *Adv. Sens. Energy Mater.* **2023**, *2*, 100069. [CrossRef]
39. Chowdhury, A.P.; Anantharaju, K.S.; Keshavamurthy, K.; Rokhum, S.L. Recent Advances in Efficient Photocatalytic Degradation Approaches for Azo Dyes. *J. Chem.* **2023**, *2023*, 9780955. [CrossRef]
40. Perera, H.; Gurunanthanan, V.; Singh, A.; Mantilaka, M.; Das, G.; Arya, S. Magnesium oxide (MgO) nanoadsorbents in wastewater treatment: A comprehensive review. *J. Magnes. Alloys* **2024**, *12*, 1709–1773. [CrossRef]
41. Roozbahani, P.A.; Behnejad, H.; Hamzehloo, M. Synthesis, analysis, and application of zinc oxide and bismuth-based nanocomposites (ZnO/$BaBi_2O_6$) as a photocatalyst for organic dyes degradation. *Inorg. Chem. Commun.* **2024**, *168*, 112821. [CrossRef]
42. Angelé-Martínez, C.; Nguyen, K.V.T.; Ameer, F.S.; Anker, J.N.; Brumaghim, J.L. Reactive Oxygen Species Generation by Copper(II) Oxide Nanoparticles Determined by DNA Damage Assays and EPR Spectroscopy. *Nanotoxicology* **2017**, *11*, 278–288. [CrossRef] [PubMed]
43. Khan, M.A.; Safira, A.R.; Kaseem, M.; Fattah-Alhosseini, A. Enhanced electrochemical and photocatalytic performance achieved through dual incorporation of SnO_2 and WO_3 nanoparticles into LDH layer fabricated on PEO-coated AZ31 Mg alloy. *J. Magnes. Alloys* **2024**, *12*, 1880–1898. [CrossRef]
44. Singh, K.R.; Nayak, V.; Singh, J.; Singh, A.K.; Singh, R.P. Potentialities of bioinspired metal and metal oxide nanoparticles in biomedical sciences. *RSC Adv.* **2021**, *11*, 24722–24746. [CrossRef] [PubMed]
45. Raizada, P.; Sudhaik, A.; Patial, S.; Hasija, V.; Khan, A.A.P.; Singh, P.; Gautam, S.; Kaur, M.; Nguyen, V.-H. Engineering nanostructures of CuO-based photocatalysts for water treatment: Current progress and future challenges. *Arab. J. Chem.* **2020**, *13*, 8424–8457. [CrossRef]
46. Sahu, K.; Bisht, A.; Kuriakose, S.; Mohapatra, S. Two-dimensional CuO-ZnO nanohybrids with enhanced photocatalytic performance for removal of pollutants. *J. Phys. Chem. Solids* **2020**, *137*, 109223. [CrossRef]
47. Fouda, A.; Salem, S.S.; Wassel, A.R.; Hamza, M.F.; Shaheen, T. Optimization of green biosynthesized visible light active CuO/ZnO nano-photocatalysts for the degradation of organic methylene blue dye. *Heliyon* **2020**, *6*, e04896. [CrossRef]
48. Hassaan, M.A.; El-Nemr, M.A.; Elkatory, M.R.; Ragab, S.; Niculescu, V.C.; El Nemr, A. Principles of Photocatalysts and Their Different Applications: A Review. *Top. Curr. Chem.* **2023**, *381*, 31. [CrossRef] [PubMed]
49. Ma, G. Three common preparation methods of hydroxyapatite. *IOP Conf. Ser. Mater. Sci. Eng.* **2019**, *688*, 033057. [CrossRef]
50. Kadam, A.V.; Bhosale, N.Y.; Patil, S.B.; Mali, S.S.; Hong, C.K. Fabrication of an electrochromic device by using WO_3 thin films synthesized using facile single-step hydrothermal process. *Thin Solid Films* **2019**, *673*, 86–93. [CrossRef]
51. Bouras, D.; Mecif, A.; Barillé, R.; Harabi, A.; Rasheed, M.; Mahdjoub, A.; Zaabat, M. Cu:ZnO deposited on porous ceramic substrates by a simple thermal method for photocatalytic application. *Ceram. Int.* **2018**, *44*, 21546–21555. [CrossRef]
52. Bouras, D.; Mecif, A.; Harabi, A.; Barillé, R.; Mahdjoub, A.H.; Zaabat, M. Economic and ultrafast photocatalytic degradation of orange II using ceramic powders. *Catalysts* **2021**, *11*, 733. [CrossRef]
53. Bouras, D.; Fellah, M.; Mecif, A.; Barillé, R.; Obrosov, A.; Rasheed, M. High photocatalytic capacity of porous ceramic-based powder doped with MgO. *J. Korean Ceram. Soc.* **2023**, *60*, 155–168. [CrossRef]
54. Bouras, D.; Mecif, A.; Barillé, R.; Harabi, A.; Zaabat, M. Porosity properties of porous ceramic substrates added with zinc and magnesium material. *Ceram. Int.* **2020**, *46*, 20838–20846. [CrossRef]
55. Buyakov, A.; Shmakov, V.; Zabolotsky, A.; Chumakov, Y.; Shilko, E. Refractory ceramics based on magnesium–aluminate spinel and periclase of the Satka deposit. *Mater. Chem. Phys.* **2024**, *313*, 128760. [CrossRef]

56. Barman, S.; Sikdar, S.; Das, R. A comprehensive study on ZrO_2-ZnO nanocomposites synthesized by the plant-mediated green method. *Phys. Scr.* **2023**, *98*, 085947. [CrossRef]
57. Mureddu, M.; Ferrara, F.; Pettinau, A. Highly efficient CuO/ZnO/ZrO_2@SBA-15 nanocatalysts for methanol synthesis from the catalytic hydrogenation of CO_2. *Appl. Catal. B Environ.* **2019**, *258*, 117941. [CrossRef]
58. L'hospital, V.; Angelo, L.; Zimmermann, Y.; Parkhomenko, K.; Roger, A.-C. Influence of the Zn/Zr ratio in the support of a copper-based catalyst for the synthesis of methanol from CO_2. *Catal. Today* **2021**, *369*, 95–104. [CrossRef]
59. Quintana, A.; Altube, A.; García-Lecina, E.; Suriñach, S.; Baró, M.D.; Sort, J.; Pellicer, E.; Guerrero, M. A facile co-precipitation synthesis of heterostructured ZrO_2 | ZnO nanoparticles as efficient photocatalysts for wastewater treatment. *J. Mater. Sci.* **2017**, *52*, 13779–13789. [CrossRef]
60. Benrezgua, E.; Deghfel, B.; Zoukel, A.; Basirun, W.J.; Amari, R.; Boukhari, A.; Yaakob, M.K.; Kheawhom, S.; Mohamad, A.A. Synthesis and properties of copper doped zinc oxide thin films by sol-gel, spin coating and dipping: A characterization review. *J. Mol. Struct.* **2022**, *1267*, 133639. [CrossRef]
61. Jeevan, S.; Venkatachalam, M.; Manickam, M.S. ZNO Thin Film Prepared by Dip Coating Technique for Gas Sensing Application. *Int. J. Res. Appl. Sci. Eng. Technol.* **2017**, *5*, 417–419. [CrossRef]
62. Ben Saad, L.; Soltane, L.; Sediri, F. Pure and Cu-Doped ZnO Nanoparticles: Hydrothermal Synthesis, Structural, and Optical Properties. *Russ. J. Phys. Chem. A* **2019**, *93*, 2782–2788. [CrossRef]
63. Singh, A.; Ahmed, A.; Sharma, A.; Sharma, C.; Paul, S.; Khosla, A.; Gupta, V.; Arya, S. Promising photocatalytic degradation of methyl orange dye via sol-gel synthesized Ag–CdS@Pr-TiO_2 core/shell nanoparticles. *Phys. B Condens. Matter* **2021**, *616*, 413121. [CrossRef]
64. di Confiengo, G.G.; Faga, M.G.; La Parola, V.; Magnacca, G.; Paganini, M.C.; Testa, M.L. Microwave approach and thermal decomposition: A sustainable way to produce ZnO nanoparticles with different chemo-physical properties. *Mater. Chem. Phys.* **2024**, *321*, 129485. [CrossRef]
65. Myślińska, M.; Stocker, M.W.; Ferguson, S.; Healy, A.M. A Comparison of Spray-Drying and Co-Precipitation for the Generation of Amorphous Solid Dispersions (ASDs) of Hydrochlorothiazide and Simvastatin. *J. Pharm. Sci.* **2023**, *112*, 2097–2114. [CrossRef] [PubMed]
66. Aidhy, D.S.; Liu, B.; Zhang, Y.; Weber, W.J. Chemical expansion affected oxygen vacancy stability in different oxide structures from first principles calculations. *Comput. Mater. Sci.* **2015**, *99*, 298–305. [CrossRef]
67. Magomedov, M. On the deviation from the Vegard's law for the solid solutions. *Solid State Commun.* **2020**, *322*, 114060. [CrossRef]
68. Awasthi, S.; Moharana, S.; Kumar, V.; Wang, N.; Chmanehpour, E.; Sharma, A.D.; Tiwari, S.K.; Kumar, V.; Mishra, Y.K. Progress in doping and crystal deformation for polyanions cathode based lithium-ion batteries. *Nano Mater. Sci.* **2024**, *6*, 504–535. [CrossRef]
69. Nyabadza, A.; McCarthy, É.; Makhesana, M.; Heidarinassab, S.; Plouze, A.; Vazquez, M.; Brabazon, D. A review of physical, chemical and biological synthesis methods of bimetallic nanoparticles and applications in sensing, water treatment, biomedicine, catalysis and hydrogen storage. *Adv. Colloid Interface Sci.* **2023**, *321*, 103010. [CrossRef]
70. Lim, N.Y.Y.; Chiam, S.L.; Leo, C.; Chang, C.K. Recent modification, mechanisms, and performance of zinc oxide-based photocatalysts for sustainable dye degradation. *Hybrid Adv.* **2024**, *7*, 100318. [CrossRef]
71. Alasmari, A.; Alresheedi, N.M.; Alzahrani, M.A.; Aldosari, F.M.; Ghasemi, M.; Ismail, A.; Aboraia, A.M. High-performance photocatalytic degradation—A ZnO nanocomposite co-doped with Gd: A systematic study. *Catalysts* **2024**, *14*, 946. [CrossRef]
72. El-Sayed, F.; Hussien, M.S.A.; Mohammed, M.I.; Ganesh, V.; AlAbdulaal, T.H.; Zahran, H.Y.; Yahia, I.S.; Hegazy, H.H.; Abdel-Wahab, M.S.; Shkir, M.; et al. The photocatalytic performance of Nd_2O_3 doped CuO nanoparticles with enhanced methylene blue degradation: Synthesis, characterization and comparative study. *Nanomaterials* **2022**, *12*, 1060. [CrossRef]
73. Atta, D.; Wahab, H.A.; Ibrahim, M.A.; Battisha, I.K. Photocatalytic degradation of methylene blue dye by ZnO nanoparticle thin films, using sol–gel technique and UV laser irradiation. *Sci. Rep.* **2024**, *14*, 26961. [CrossRef]
74. Mosleh, A.T.; Kamoun, E.A.; El-Moslamy, S.H.; Salim, S.A.; Zahran, H.Y.; Zyoud, S.H.; Yahia, I.S. Performance of Ag-doped CuO nanoparticles for photocatalytic activity applications: Synthesis, characterization, and antimicrobial activity. *Discov. Nano* **2024**, *19*, 166. [CrossRef] [PubMed]
75. Bouras, D.; Rasheed, M. Comparison between CrZO and AlZO thin layers and the effect of doping on the lattice properties of zinc oxide. *Opt. Quantum Electron.* **2022**, *54*, 824. [CrossRef]
76. Karthik, K.; Raghu, A.; Reddy, K.R.; Ravishankar, R.; Sangeeta, M.; Shetti, N.P.; Reddy, C.V. Green synthesis of Cu-doped ZnO nanoparticles and its application for the photocatalytic degradation of hazardous organic pollutants. *Chemosphere* **2022**, *287*, 132081. [CrossRef]
77. Barranco, A.; Borras, A.; Gonzalez-Elipe, A.R.; Palmero, A. Perspectives on oblique angle deposition of thin films: From fundamentals to devices. *Prog. Mater. Sci.* **2016**, *76*, 59–153. [CrossRef]
78. Iribarren, A.; Hernández-Rodríguez, E.; Maqueira, L. Structural, chemical and optical evaluation of Cu-doped ZnO nanoparticles synthesized by an aqueous solution method. *Mater. Res. Bull.* **2014**, *60*, 376–381. [CrossRef]

79. Wang, E.A.; Hong, C.S.; Shavat, S.; Kessell, E.R.; Sanders, R.; Kushel, M.B. Wang et al. Respond. *Am. Public Health Assoc.* **2013**, *103*, e6–e7. [CrossRef]
80. Muchuweni, E.; Sathiaraj, T.; Nyakotyo, H. Synthesis and characterization of zinc oxide thin films for optoelectronic applications. *Heliyon* **2017**, *3*, e00285. [CrossRef]
81. Quy, B.M.; Thu, N.T.N.; Xuan, V.T.; Hoa, N.T.H.; Linh, N.T.N.; Tung, V.Q.; Le, V.T.T.; Thao, T.T.; Ngan, N.T.K.; Tho, P.T.; et al. Photocatalytic degradation performance of a chitosan/ZnO–Fe_3O_4 nanocomposite over cationic and anionic dyes under visible-light irradiation. *RSC Adv.* **2025**, *15*, 1590–1603. [CrossRef]
82. Saha, H.; Dastider, A.; Anik, J.F.; Mim, S.R.; Talapatra, S.; Das, U.; Jamal, M.; Billah, M. Photocatalytic performance of CuO NPs: An experimental approach for process parameter optimization for Rh B dye. *Results Mater.* **2024**, *24*, 100614. [CrossRef]
83. Aroob, S.; Carabineiro, S.A.C.; Taj, M.B.; Bibi, I.; Raheel, A.; Javed, T.; Yahya, R.; Alelwani, W.; Verpoort, F.; Kamwilaisak, K.; et al. Green synthesis and photocatalytic dye degradation activity of CuO nanoparticles. *Catalysts* **2023**, *13*, 502. [CrossRef]
84. Ahmadpour, G.; Nilforoushan, M.R.; Boroujeny, B.S.; Tayebi, M.; Jesmani, S.M. Effect of substrate surface treatment on the hydrothermal synthesis of zinc oxide nanostructures. *Ceram. Int.* **2022**, *48*, 2323–2329. [CrossRef]
85. Dursun, S.; Koyuncu, S.N.; Kaya, I.C.; Kaya, G.G.; Kalem, V.; Akyildiz, H. Production of CuO–WO_3 hybrids and their dye removal capacity/performance from wastewater by adsorption/photocatalysis. *J. Water Process. Eng.* **2020**, *36*, 101390. [CrossRef]
86. Tahir, H.; Anwer, M.; Khan, S.; Saad, M. Enhancement of adsorption and photocatalytic activity of MgO nanoparticles for the treatment of textile dye using ultrasound assisted process by Response Surface Methodology. *Desalination Water Treat.* **2024**, *319*, 100429. [CrossRef]
87. Gatou, M.-A.; Bovali, N.; Lagopati, N.; Pavlatou, E.A. MgO nanoparticles as a promising photocatalyst towards rhodamine B and rhodamine 6G degradation. *Molecules* **2024**, *29*, 4299. [CrossRef]
88. Singaram, G.M.P.; Selvaraj, R. Photocatalytic degradation of acid violet dye by sunlight exposure using green synthesized magnesium oxide nanoparticles. *Chem. Phys. Impact* **2024**, *8*, 100628. [CrossRef]
89. Elashery, S.E.A.; Ibrahim, I.; Gomaa, H.; El-Bouraie, M.M.; Moneam, I.A.; Fekry, S.S.; Mohamed, G.G. Comparative study of the photocatalytic degradation of crystal violet using ferromagnetic magnesium oxide nanoparticles and MgO-bentonite nanocomposite. *Magnetochemistry* **2023**, *9*, 56. [CrossRef]
90. Devi, P.G.; Velu, A.S. Synthesis, structural and optical properties of pure ZnO and Co doped ZnO nanoparticles prepared by the co-precipitation method. *J. Theor. Appl. Phys.* **2016**, *10*, 233–240. [CrossRef]
91. Khan, I.; Saeed, K.; Khan, I. Nanoparticles: Properties, applications and toxicities. *Arab. J. Chem.* **2019**, *12*, 908–931. [CrossRef]
92. Bano, K.; Kaushal, S.; Lal, B.; Joshi, S.K.; Kumar, R.; Singh, P.P. Fabrication of CuO/ZnO heterojunction photocatalyst for efficient photocatalytic degradation of tetracycline and ciprofloxacin under direct sun light. *Environ. Nanotechnol. Monit. Manag.* **2023**, *20*, 100863. [CrossRef]
93. Anaya-Esparza, L.M.; Montalvo-González, E.; González-Silva, N.; Méndez-Robles, M.D.; Romero-Toledo, R.; Yahia, E.M.; Pérez-Larios, A. Synthesis and Characterization of TiO_2-ZnO-MgO Mixed Oxide and Their Antibacterial Activity. *Materials* **2019**, *12*, 698. [CrossRef]
94. Lee, D.-E.; Kim, M.-K.; Danish, M.; Jo, W.-K. State-of-the-art review on photocatalysis for efficient wastewater treatment: Attractive approach in photocatalyst design and parameters affecting the photocatalytic degradation. *Catal. Commun.* **2023**, *183*, 106764. [CrossRef]
95. Zhou, H.; Wang, H.; Yue, C.; He, L.; Li, H.; Zhang, H.; Yang, S.; Ma, T. Photocatalytic degradation by TiO_2-conjugated/coordination polymer heterojunction: Preparation, mechanisms, and prospects. *Appl. Catal. B Environ. Energy* **2023**, *344*, 123605. [CrossRef]
96. Fellah, M.; Hezil, N.; Bouras, D.; Habeeb, M.A.; Hamadi, F.; Bouchareb, N.; Laouini, S.E.; Larios, A.P.; Aleksei, O.; El-Hiti, G.A. Microstructural and photocatalytic properties of nanostructured near-β Ti-Nb-Zr alloy for total hip prosthesis use. *Kuwait J. Sci.* **2024**, *51*, 100276. [CrossRef]
97. Kefeni, K.K.; Mamba, B.B. Photocatalytic application of spinel ferrite nanoparticles and nanocomposites in wastewater treatment: Review. *Sustain. Mater. Technol.* **2020**, *23*, e00140. [CrossRef]
98. Ren, G.; Han, H.; Wang, Y.; Liu, S.; Zhao, J.; Meng, X.; Li, Z. Recent Advances of Photocatalytic Application in Water Treatment: A Review. *Nanomaterials* **2021**, *11*, 1804. [CrossRef]
99. Rani, V.; Malhotra, M.; Patial, S.; Sharma, S.; Singh, P.; Khan, A.A.P.; Thakur, S.; Raizada, P.; Ahamad, T.; Asiri, A.M. Formulation strategies for the photocatalytic H_2 evolution and photodegradation using MoO3-based Z-scheme photocatalysts. *Mater. Chem. Phys.* **2023**, *299*, 127454. [CrossRef]
100. Deshpande, B.; Agrawal, P.; Yenkie, M.; Dhoble, S. Prospective of nanotechnology in degradation of waste water: A new challenges. *Nano-Struct. Nano-Objects* **2020**, *22*, 100442. [CrossRef]
101. Bouras, D.; Rasheed, M.; Barille, R.; Aldaraji, M.N. Efficiency of adding DD3+(Li/Mg) composite to plants and their fibers during the process of filtering solutions of toxic organic dyes. *Opt. Mater.* **2022**, *131*, 112725. [CrossRef]

102. Khader, E.H.; Muslim, S.A.; Saady, N.M.C.; Ali, N.S.; Salih, I.K.; Mohammed, T.J.; Albayati, T.M.; Zendehboudi, S. Recent advances in photocatalytic advanced oxidation processes for organic compound degradation: A review. *Desalination Water Treat.* **2024**, *318*, 100384. [CrossRef]
103. Ge, J.; Zhang, Y.; Heo, Y.-J.; Park, S.-J. Advanced Design and Synthesis of Composite Photocatalysts for the Remediation of Wastewater: A Review. *Catalysts* **2019**, *9*, 122. [CrossRef]
104. Ahamad, T.; Naushad, M.; Eldesoky, G.E.; Al-Saeedi, S.I.; Nafady, A.; Al-Kadhi, N.S.; Al-Muhtaseb, A.H.; Khan, A.A.; Khan, A. Effective and fast adsorptive removal of toxic cationic dye (MB) from aqueous medium using amino-functionalized magnetic multiwall carbon nanotubes. *J. Mol. Liq.* **2019**, *282*, 154–161. [CrossRef]
105. Kunde, S.P.; Kanade, K.G.; Karale, B.K.; Akolkar, H.N.; Randhavane, P.V.; Shinde, S.T. Synthesis and characterization of nanostructured Cu-ZnO: An efficient catalyst for the preparation of (E)-3-styrylchromones. *Arab. J. Chem.* **2019**, *12*, 5212–5222. [CrossRef]
106. Vaiano, V.; Chianese, L.; Rizzo, L.; Iervolino, G. Visible light driven oxidation of arsenite to arsenate in aqueous solution using Cu-doped ZnO supported on polystyrene pellets. *Catal. Today* **2021**, *361*, 69–76. [CrossRef]
107. Pavel, M.; Anastasescu, C.; State, R.-N.; Vasile, A.; Papa, F.; Balint, I. Photocatalytic Degradation of Organic and Inorganic Pollutants to Harmless End Products: Assessment of Practical Application Potential for Water and Air Cleaning. *Catalysts* **2023**, *13*, 380. [CrossRef]
108. Singh, A.; Dhau, J.; Kumar, R.; Badru, R.; Singh, P.; Mishra, Y.K.; Kaushik, A. Tailored carbon materials (TCM) for enhancing photocatalytic degradation of polyaromatic hydrocarbons. *Prog. Mater. Sci.* **2024**, *144*, 101289. [CrossRef]
109. Anucha, C.B.; Altin, I.; Bacaksiz, E.; Stathopoulos, V.N. Titanium dioxide (TiO_2)-based photocatalyst materials activity enhancement for contaminants of emerging concern (CECs) degradation: In the light of modification strategies. *Chem. Eng. J. Adv.* **2022**, *10*, 100262. [CrossRef]
110. Parambil, N.S.K.; Raphael, S.J.; Joseph, P.; Dasan, A. Recent advancements toward visible-light-driven titania-based nanocomposite systems for environmental applications: An overview. *Appl. Surf. Sci. Adv.* **2023**, *18*, 100487. [CrossRef]
111. Bhunia, A.; Studer, A. Recent advances in radical chemistry proceeding through pro-aromatic radicals. *Chem* **2021**, *7*, 2060–2100. [CrossRef]
112. Kumari, P.; Kumar, A. ADVANCED OXIDATION PROCESS: A remediation technique for organic and non-biodegradable pollutant. *Results Surf. Interfaces* **2023**, *11*, 100122. [CrossRef]
113. Camargo-Perea, A.L.; Serna-Galvis, E.A.; Lee, J.; Torres-Palma, R.A. Understanding the effects of mineral water matrix on degradation of several pharmaceuticals by ultrasound: Influence of chemical structure and concentration of the pollutants. *Ultrason. Sonochem.* **2021**, *73*, 105500. [CrossRef] [PubMed]
114. Riquelme, C.; Gómez, G.; Vidal, G.; Neumann, P. Critical analysis of the performance of pilot and industrial scale technologies for sewage reuse. *J. Environ. Chem. Eng.* **2022**, *10*, 108198. [CrossRef]
115. Sepman, H.; Malm, L.; Peets, P.; Kruve, A. Scientometric review: Concentration and toxicity assessment in environmental non-targeted LC/HRMS analysis. *Trends Environ. Anal. Chem.* **2023**, *40*, e00217. [CrossRef]
116. Ranjbari, A.; Kim, J.; Yu, J.; Kim, J.; Park, M.; Kim, N.; Demeestere, K.; Heynderickx, P.M. Effect of oxygen vacancy modification of ZnO on photocatalytic degradation of methyl orange: A kinetic study. *Catal. Today* **2024**, *427*, 114413. [CrossRef]
117. Akhter, P.; Nawaz, S.; Shafiq, I.; Nazir, A.; Shafique, S.; Jamil, F.; Park, Y.-K.; Hussain, M. Efficient visible light assisted photocatalysis using ZnO/TiO_2 nanocomposites. *Mol. Catal.* **2023**, *535*, 112896. [CrossRef]
118. Al-Rawashdeh, N.A.F.; Allabadi, O.; Aljarrah, M.T. Photocatalytic activity of graphene oxide/zinc oxide nanocomposites with embedded metal nanoparticles for the degradation of organic dyes. *ACS Omega* **2020**, *5*, 28046–28055. [CrossRef]
119. Velusamy, S.; Roy, A.; Mariam, E.; Krishnamurthy, S.; Sundaram, S.; Mallick, T.K. Effectual visible light photocatalytic reduction of para-nitro phenol using reduced graphene oxide and ZnO composite. *Sci. Rep.* **2023**, *13*, 9521. [CrossRef]
120. Bouchareb, N.; Fellah, M.; Hezil, N.; Hamadi, F.; Montagne, A.; Obrosov, A.; Yadav, K.; El-Hiti, G.A. Effect of milling time on structural, physical and photocatalytical properties of Ti-Ni alloy for biomedical applications. *Int. J. Adv. Manuf. Technol.* **2024**, *131*, 3539–3553. [CrossRef]
121. Paniagua-Méndez, J.; Ramírez-Sandoval, S.; Reyes-Uribe, E.; Contreras-García, M. Photocatalytic activity and biocide effect of nanostructured $SnO_2/ZnO/TiO_2$ thin film heterostructure obtained by sol-gel spin coating technique. *Ceram. Int.* **2024**, *50*, 34421–34430. [CrossRef]
122. Estrella-Pajulas, L.L.; Gamala, B.J.I. A review on the synthesis, characterization, and recent advancements of visible light-activated C-TiO_2 nanomaterials for environmental remediation. *Next Nanotechnol.* **2024**, *6*, 100082. [CrossRef]
123. Arumugham, N.; Mariappan, A.; Eswaran, J.; Daniel, S.; Kanthapazham, R.; Kathirvel, P. Nickel ferrite-based composites and its photocatalytic application—A review. *J. Hazard. Mater. Adv.* **2022**, *8*, 100156. [CrossRef]
124. Shokraiyan, J.; Asadi, M.; Rabbani, M. A Comparison of photocatalytic activity of CuO, ZnO, and ZnO/CuO nanocomposites for degrading water pollutants under LED light. *Chem. Data Collect.* **2021**, *34*, 100747. [CrossRef]

125. Çinar, B.; Kerimoğlu, I.; Tönbül, B.; Demirbüken, A.; Dursun, S.; Kaya, I.C.; Kalem, V.; Akyildiz, H. Hydrothermal/electrospinning synthesis of CuO plate-like particles/TiO_2 fibers heterostructures for high-efficiency photocatalytic degradation of organic dyes and phenolic pollutants. *Mater. Sci. Semicond. Process.* **2020**, *109*, 104919. [CrossRef]
126. Hassan, Q.; Algburi, S.; Sameen, A.Z.; Salman, H.M.; Jaszczur, M. Green hydrogen: A pathway to a sustainable energy future. *Int. J. Hydrogen Energy* **2024**, *50*, 310–333. [CrossRef]
127. Cai Ng, W.; Siang Yaw, C.; Amira Shaffee, S.N.; Abd Samad, N.A.; Koi, Z.K.; Chong, M.N. Elevating the prospects of green hydrogen (H_2) production through solar-powered water splitting devices: A systematic review. *Sustain. Mater. Technol.* **2024**, *40*, e00972. [CrossRef]
128. Boddula, R.; Lee, Y.-Y.; Masimukku, S.; Chang-Chien, G.-P.; Pothu, R.; Srivastava, R.K.; Sarangi, P.K.; Selvaraj, M.; Basumatary, S.; Al-Qahtani, N. Sustainable hydrogen production: Solar-powered biomass conversion explored through (Photo)electrochemical advancements. *Process. Saf. Environ. Prot.* **2024**, *18*, 1149–1168. [CrossRef]
129. Nayak, S.; Parida, K. MgCr-LDH Nanoplatelets as Effective Oxidation Catalysts for Visible Light-Triggered Rhodamine B Degradation. *Catalysts* **2021**, *11*, 1072. [CrossRef]
130. Jia, J.; Zhang, Q.; Li, Z.; Hu, X.; Liu, E.; Fan, J. Lateral heterojunctions within ultrathin FeS–$FeSe_2$ nanosheet semiconductors for photocatalytic hydrogen evolution. *J. Mater. Chem. A* **2019**, *7*, 3828–3841. [CrossRef]
131. Li, X.; Chen, Y.; Tao, Y.; Shen, L.; Xu, Z.; Bian, Z.; Li, H. Challenges of photocatalysis and their coping strategies. *Chem Catal.* **2022**, *2*, 1315–1345. [CrossRef]
132. Lei, R.; Zhang, H.; Ni, H.; Chen, R.; Gu, H.; Zhang, B. Novel ZnO nanoparticles modified WO_3 nanosheet arrays for enhanced photocatalytic properties under solar light illumination. *Appl. Surf. Sci.* **2019**, *463*, 363–373. [CrossRef]
133. Reghunath, S.; Pinheiro, D.; Kr, S.D. A review of hierarchical nanostructures of TiO_2: Advances and applications. *Appl. Surf. Sci. Adv.* **2021**, *3*, 100063. [CrossRef]
134. Gao, X.; Li, L.; An, M.; Zheng, T.; Ma, F. ZnO QDs and three-dimensional ordered macroporous structure synergistically enhance the photocatalytic degradation and hydrogen evolution performance of WO_3/TiO_2 composites. *J. Phys. Chem. Solids* **2022**, *165*, 110655. [CrossRef]
135. Chaudhary, D.; Singh, S.; Vankar, V.; Khare, N. ZnO nanoparticles decorated multi-walled carbon nanotubes for enhanced photocatalytic and photoelectrochemical water splitting. *J. Photochem. Photobiol. A Chem.* **2018**, *351*, 154–161. [CrossRef]
136. Ruan, S.; Huang, W.; Zhao, M.; Song, H.; Gao, Z. A Z-scheme mechanism of the novel ZnO/CuO n-n heterojunction for photocatalytic degradation of Acid Orange 7. *Mater. Sci. Semicond. Process.* **2020**, *107*, 104835. [CrossRef]
137. Ding, W.; Zhao, L.; Yan, H.; Wang, X.; Liu, X.; Zhang, X.; Huang, X.; Hang, R.; Wang, Y.; Yao, X.; et al. Bovine serum albumin assisted synthesis of Ag/Ag_2O/ZnO photocatalyst with enhanced photocatalytic activity under visible light. *Colloids Surf. A Physicochem. Eng. Asp.* **2019**, *568*, 131–140. [CrossRef]
138. Zhang, Y.; Su, P.; Weathersby, D.; Zhang, Q.; Zheng, J.; Fan, R.; Zhang, J.; Dai, Q. Synthesis of γ-Fe_2O_3-ZnO-biochar nanocomposites for Rhodamine B removal. *Appl. Surf. Sci.* **2020**, *501*, 144217. [CrossRef]
139. Song, J.; Sun, G.; Yu, J.; Si, Y.; Ding, B. Construction of ternary Ag@ZnO/TiO_2 fibrous membranes with hierarchical nanostructures and mechanical flexibility for water purification. *Ceram. Int.* **2020**, *45*, 468–475. [CrossRef]
140. Wang, R.; Cao, J.; Liu, J.; Zhang, Y. Synthesis of CuO@TiO_2 nanocomposite and its photocatalytic and electrochemical properties. Application for treatment of azo dyes in industrial wastewater. *Int. J. Electrochem. Sci.* **2023**, *18*, 100316. [CrossRef]
141. Bouchareb, N.; Hezil, N.; Hamadi, F.; Fellah, M. Effect of milling time on structural, mechanical and tribological behavior of a newly developed Ti-Ni alloy for biomedical applications. *Mater. Today Commun.* **2024**, *38*, 108201. [CrossRef]

Disclaimer/Publisher's Note: The statements, opinions and data contained in all publications are solely those of the individual author(s) and contributor(s) and not of MDPI and/or the editor(s). MDPI and/or the editor(s) disclaim responsibility for any injury to people or property resulting from any ideas, methods, instructions or products referred to in the content.